

## Three-dimensional magnetotelluric characterization of the Coso geothermal field

Gregory A. Newman<sup>a,\*</sup>, Erika Gasperikova<sup>a</sup>,  
G. Michael Hoversten<sup>b</sup>, Philip E. Wannamaker<sup>c</sup>

<sup>a</sup> *Lawrence Berkeley National Laboratory, Earth Sciences Division,  
Berkeley, CA 94720, USA*

<sup>b</sup> *Chevron Energy Technology Company, Seismic Analysis and Property Estimation,  
San Ramon, CA 94583, USA*

<sup>c</sup> *Energy and Geoscience Institute, University of Utah, Salt Lake City,  
UT 84108, USA*

Received 4 February 2008; accepted 5 February 2008

Available online 14 April 2008

### Abstract

A dense grid of 125 magnetotelluric (MT) stations plus a single line of contiguous bipole array profiling has been acquired over the east flank of the Coso geothermal system, CA, USA. Due to production related electromagnetic (EM) noise the permanent observatory at Parkfield, CA was used as a remote reference to suppress this cultural EM noise interference. These data have been inverted to a fully three-dimensional (3D) resistivity model. This model shows the controlling geological structures possibly influencing well production at Coso and correlations with mapped surface features such as faults and the regional geoelectric strike. The 3D model also illustrates the refinement in positioning of resistivity contacts when compared to isolated 2D inversion transects. The resistivity model has also been correlated with micro-earthquake locations, reservoir fluid production intervals and most importantly with an acoustic and shear velocity model derived by Wu and Lees [Wu, H., Lees, J.M., 1999. Three-dimensional *P* and *S* wave velocity structures of the Coso Geothermal Area, California, from microseismic travel time data. *J. Geophys. Res.* 104 (B6), 13217–13233]. This later correlation shows that the near-vertical low-resistivity structure on the eastern flank of the producing field is also a zone of increased acoustic velocity and increased  $V_p/V_s$  ratio bounded by mapped fault traces. Over of the Devils' Kitchen is an area of large geothermal well density, where highly conductive near surface material is interpreted as a smectite clay cap alteration zone manifested from the subsurface geothermal fluids and related geochemistry. Enhanced resistivity beneath this cap and within the reservoir is diagnostic of propylitic alteration causing the formation of illite clays, which is typically observed in high-temperature reservoirs (>230 °C). In the southwest flank of the field the  $V_p/V_s$  ratio is enhanced over the production

\* Corresponding author. Tel.: +1 510 486 6887; fax: +1 510 486 5686.

E-mail address: [gnewman@lbl.gov](mailto:gnewman@lbl.gov) (G.A. Newman).

intervals, but the resistivity is non-descript. It is recommended that more MT data sites be acquired to the south and southwest of Devil's Kitchen to better refine the resistivity model in this area.

© 2008 Elsevier Ltd. All rights reserved.

**Keywords:** Geothermal resource characterization; 3D magnetotellurics; Coso; USA

---

## 1. Introduction

Several geophysical techniques can be used to image the subsurface of a geothermal system and determine its geometry and physical properties. Such information is critical in characterizing the geologic structures that control geothermal fluid flow. The most commonly imaged rock properties are seismic velocity (acoustic and shear), density and electrical resistivity.

The degree to which a geophysical technique can be used successfully to infer geothermal reservoir properties (fracture orientation, fracture density, temperature and fluid saturations) depends on how uniquely the reservoir parameters are related to the geophysical parameters. Because these relationships are often not unique (high water saturation (brines) and high clay content both produce low electrical resistivity) it may be necessary to integrate multiple techniques to better interpret reservoir parameters from geophysical data (cf. [Garg et al., 2007](#)). In this paper we describe the application of magnetotellurics (MT) at the Coso geothermal field and show the correlations (or lack thereof) between the derived electrical parameters and seismic velocity from other experiments.

Magnetotelluric methods have been used in geothermal exploration since the early 1980s. Recently, the introduction of distributed computing has allowed the realistic modeling and inversion of three-dimensional (3D) MT data leading to the characterization of the electrical structure of geothermal reservoirs in a single self-consistent manner at presumably optimal accuracy and resolution. Here, we will test this assumption on MT data acquired over the eastern and southern flank of the Coso geothermal field (USA) and investigate whether 3D modeling and imaging can avoid artifacts inherent in 2D data analysis. Demonstrating this in the geothermal context may advance MT characterization of geothermal systems beyond the current state and show how this approach may provide useful information for siting geothermal wells.

## 2. Coso geothermal field—Geological setting

The Coso geothermal area ([Fig. 1](#)) is located in the Coso Range at the margin between the eastern flank of the Sierra Nevada and the western edge of the Basin and Range tectonic province of southeastern California, and lies within the Walker Lane/Eastern California Shear Zone (WLSZ) ([Fig. 2](#)). The Basin and Range province, an area of high heat flow and seismicity, is characterized by northerly trending fault-block mountains separated by valleys filled with alluvial deposits, that result from extensional tectonism. The WLSZ is a tectonically active feature and is characterized in the Coso region as accommodating approximately 11 mm/yr of N–S trending, right-lateral strike-slip motion between “stable North America” and the Sierra Nevada ([McClusky et al., 2001](#); [Dixon et al., 2000](#)). To the west, the Coso Range is separated from the Sierra Nevada by Rose Valley, the southern extension of the Owens Valley. It is bounded to the North by Owens Lake, a large saline playa. On the east, the range is bounded by Darwin (Coso) Wash and the

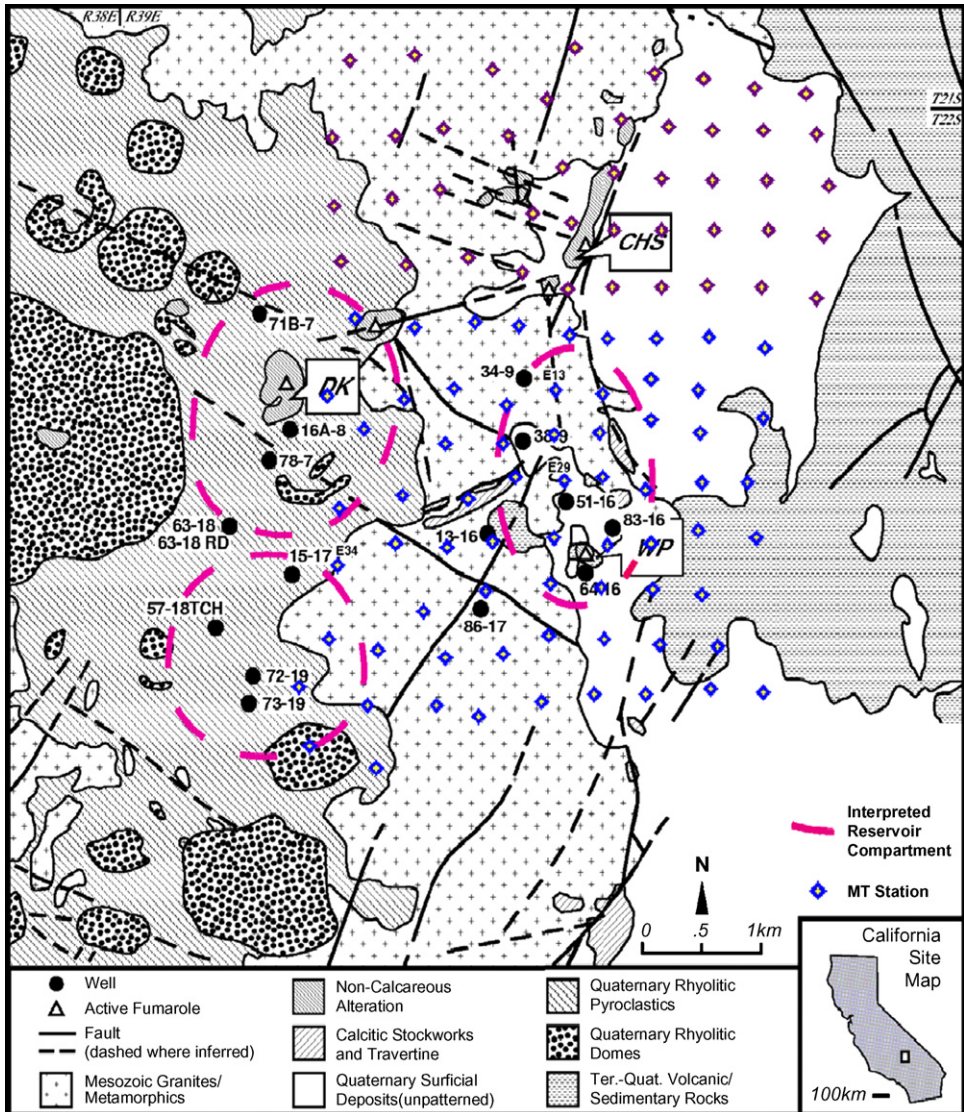


Fig. 1. Simplified geological map of the Coso geothermal area including interpreted reservoir compartmentalization (after Adams et al., 2000; Whitmarsh, 2002). Shown are the main hydrothermal alteration areas: Devil's Kitchen (DK), Coso Hot Springs (CHS), and Wheeler Prospect (WP). MT data sites acquired in 2003 are indicated by the blue and red open diamonds.

Argus Range, and on the south by Indian Wells Valley (Fig. 2); a more detailed map of active fault splays covering this region is presented in Fig. 3.

The basement of the Coso Range is dominated by fractured Mesozoic plutonic rocks with minor metamorphic rocks that have been intruded by a large number of NW trending, fine-grained dikes, and partly covered by Late Cenozoic volcanics. These dikes range in composition from felsic to mafic rocks and are believed to be part of the Independence Dike swarm of Cretaceous age. The Late Cenozoic volcanic rocks consist of basalts and rhyolites. In the last million years, during

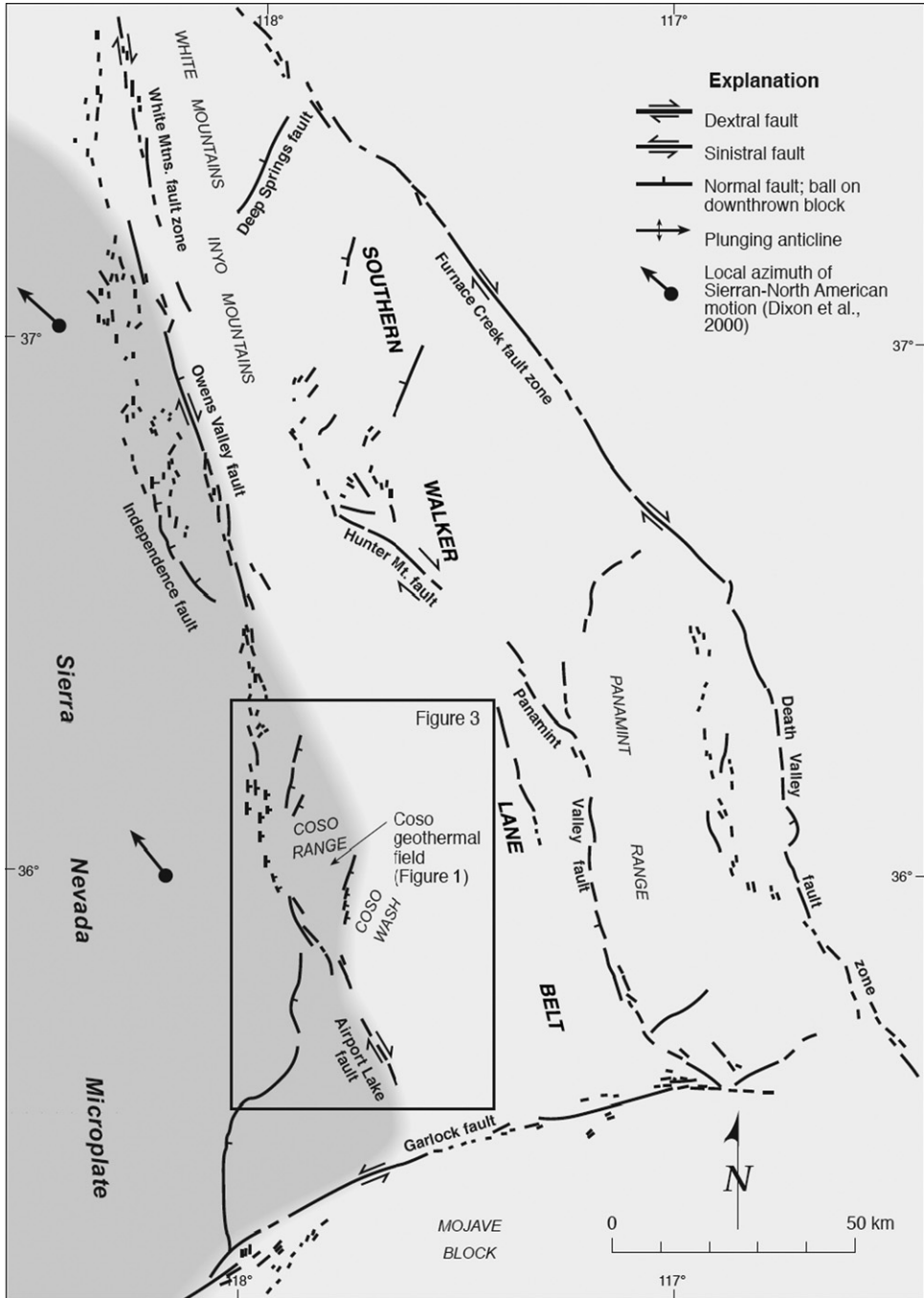


Fig. 2. Regional location map of the Coso Range and the southern Walker Lane belt. The extent of the rigid Sierra Nevada microplate is indicated by dark shading. Note right-releasing jog along the eastern margin of the Sierran microplate at the latitude of the Coso Range. The figure is from Unruh et al. (2008).



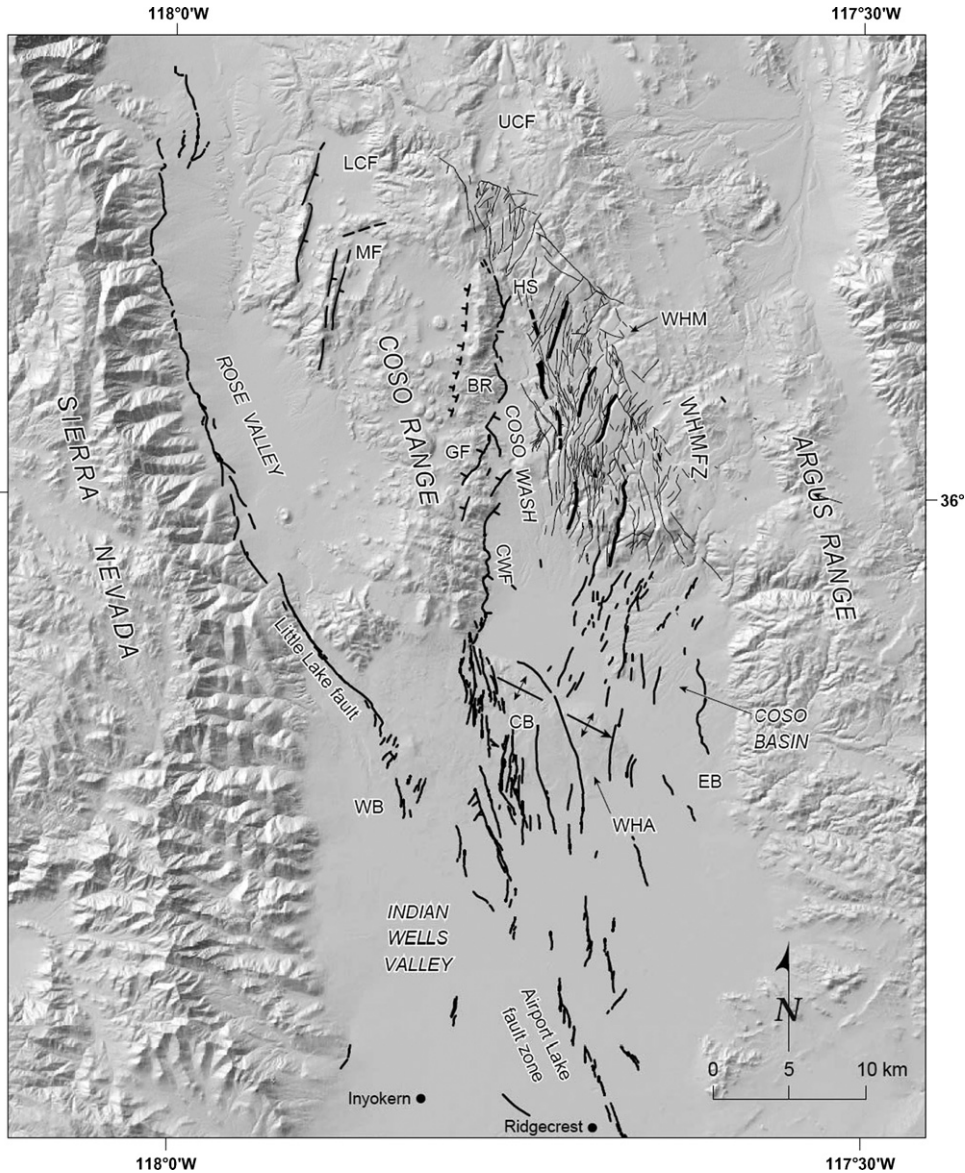


Fig. 3. Active splays of the northward branching Airport Lake Fault zone in northern Indian Wells Valley, Rose Valley, the Coso Range, and Wild Horse Mesa. Fault splays in Wild Horse Mesa with especially prominent geomorphic expression (and thus possibly accommodating greater slip) highlighted in bold. BR, Basament Ridge, CB, Central Branch, EB, Eastern Branch, CWF, Coso Wash Fault, GF, Geothermal Field, HS, Haiwee Spring, LCF, Lower Cactus Flat, MF, McCloud Flat, UCF, Upper Cactus Flat, WB, Western Branch, WHA, White Hills Anticline, WHM, Wild Horse Mesa, WHMFZ, Wild Horse Mesa Fault Zone. The figure is from Unruh et al. (2008).

the most recent volcanic phase, 39 rhyolite domes were emplaced in the central region of the field along with a relatively small amount of basalt on the margins. Over the past 600,000 years, the depth from which the rhyolites erupted has decreased, ranging from  $\sim 10$  km depth for the  $\sim 0.6$  Ma magma, to  $\sim 5.5$  km for the youngest ( $\sim 0.04$  Ma) magma. These results can be explained

by either a single rhyolitic reservoir moving upward through the crust, or a series of successively shallower reservoirs, consistent with the recent Ar–Ar geochronology (Kurilovitch et al., 2003). As the magma reservoir has become closer to the surface, eruptions have become both more frequent and more voluminous (Manley and Bacon, 2000). This partially molten magma chamber is believed to be the heat source that drives the present geothermal system.

Stresses that control the faulting and fracture permeability of the reservoir rocks are believed to be the result of the location of the Coso Range in the transitional zone between Basin and Range extensional tectonics to the east and strike-slip tectonics to the west (Roquemore, 1980; McClusky et al., 2001). Two major fault orientations have been recognized to control the geothermal system. The first set of faults strike WNW, have a vertical dip, and have strike-slip earthquake solutions, while the other strongly developed system of faults strike NNE and dip to the east. The NNE-striking fault zones have been successfully targeted in the development of the Coso geothermal field, in particular in the east flank area where wells drilled with a steep westerly dip have been the most productive (e.g. Sheridan et al., 2003).

Permeability is high within the individual Coso reservoirs but low in most of the surrounding rock, limiting reservoir fluid recharge and making reinjection important for sustained productivity. A dominantly ESE–WNW to nearly E–W extensional direction is confirmed by recent focal mechanism studies (Unruh et al., 2002). However, this extension is interpreted in the context of distributed dextral shear involving important fault zones of truly SE–NW orientation (op. cit.).

### 3. Magnetotelluric data acquisition

The magnetotelluric data acquisition was contracted to Quantec Geoscience Inc., and basics of the MT method are summarized by Vozoff (1991). A simplified cartoon of an MT site deployment as used at Coso is shown in Fig. 4. The electric ( $E$ ) and magnetic ( $H$ ) field components of the electromagnetic (EM) waves are measured with two types of sensors. The electric field is a voltage difference taken over an L-array bipole span of nominally 100 m, divided by the bipole length. Contacting endpoints of the bipoles were cold-rolled steel plates in holes approximately 20 cm

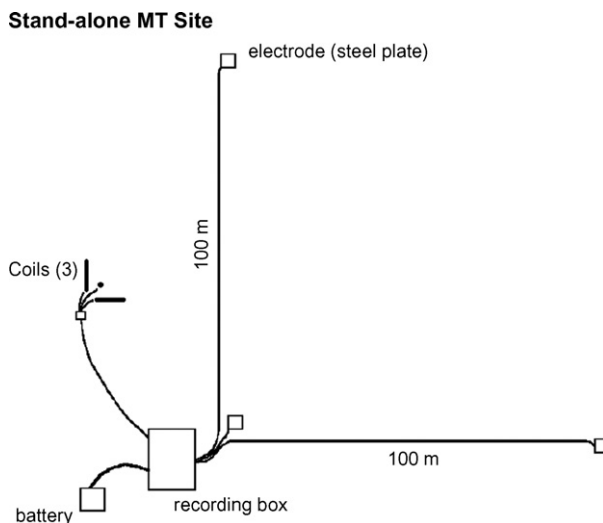


Fig. 4. Diagram of an MT station as deployed at the Coso geothermal field.

deep with about one liter of water added to improve contact. The magnetic fields were obtained using high-sensitivity solenoids (coils) with built in preamplifiers, manufactured by EMI Inc. These were buried a similar depth for thermal and mechanical stability. Due to the remote nature of the sources and the high index of refraction of the earth relative to the air, the source fields are assumed to be planar and to propagate vertically downward. However, two axes of  $E$  and three axes of  $H$  are measured because the scattering of EM waves by subsurface structure can be arbitrary in polarization, necessitating a tensor description.

Broadband EM times-series are recorded by these devices, and they are decomposed into individual frequency spectra through Fourier transformation. By way of band averaging and ratios we arrive at the tensor impedance of the earth to vertically incident, planar electromagnetic wave propagation; i.e. the fundamental MT quantity that is interpreted for geological structure. This is expressed as:

$$E = [Z]H$$

where  $Z$  is a two-rank tensor. Individual elements of the impedance are subject to simple arithmetic to obtain an apparent resistivity and impedance phase, which are more intuitive to inspect and interpret (Vozoff, 1991). The nominal frequency range recorded was from 250 to 0.01 Hz, which spans a depth range of several tens of meters to depths greater than 10 km. The assumption of a planar geometry for the MT fields is crucial in the interpretation of the data and artificial EM sources nearby can invalidate it. An obvious source could be the high-voltage, 60 Hz electrical production in the field, which may be strong enough under transmission lines or next to generation plants as to saturate MT recording electronics. Strictly speaking, however, the loss of a very narrow band of results around 60 Hz is generally not serious since the impedances are a smoothly varying function of frequency. More problematic are broadband noises whose causes are often obscure but can include power system load fluctuations (either within the Coso field or from nearby interstate transmission lines), rotating machinery, and vibration. These are especially onerous in the so-called MT “deadband”, a frequency band spanning 3–0.1 Hz, where the MT fields are particularly weak and would correspond to 2–5 km depth at which the geothermal reservoir(s) may be located.

### 3.1. “Local” remote reference processing attempts

The remote reference method (Vozoff, 1991) is designed to overcome environmental noise through coherent detection utilizing simultaneous, remotely recording sensors that are completely outside the influence of the noise sources. The reference site of course may have its own noises, but as long as these are uncorrelated with the local site, the detection principle remains valid. It is required that the remote site is of high fidelity or the final result will be degraded or a greater length of averaging time will be needed to achieve equivalent results (e.g. Egbert, 1997).

In the first Coso MT survey of 2003, reference sites were attempted at five locations of varying distance from the geothermal field (Wannamaker et al., 2004). The nearer three sites were the Centennial Flat area, Panamint Valley and Amargosa Valley, which are about 24, 48 and 100 km from the Coso field, respectively (Fig. 5). Time series from these sites were downloaded to a field computer by the local Coso collection crew for processing at essentially the same time as those in the Coso geothermal field, which is normal survey procedure. For the more distant references we discuss later, more elaborate communications procedures were required.

The MT apparent resistivities corresponding to impedance elements  $Z_{xy}$  and  $Z_{yx}$  for the reference site at Centennial Flat and in Panamint Valley are shown in Fig. 6. Characteristic of non-MT artificial effects are apparent resistivities which rise with decreasing frequency at an anomalously

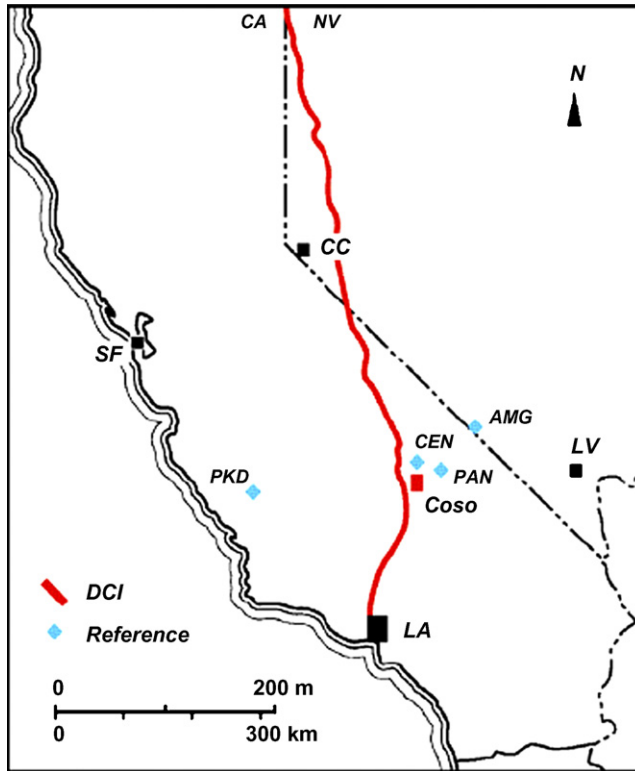


Fig. 5. Location of “remote” MT references used in the Coso MT study: Centennial Flat (CEN), Panamint Valley (PAN), Amargosa Valley (AMG) and Parkfield (PKD). Not shown is Socorro, NM, some 1000 km to the east. Also shown are the trace of the Bonneville Power Authority (BPA) DC intertie transmission line (bold red line), which was provided by Jim Lovekin, and the location of San Francisco (SF), Los Angeles (LA), Las Vegas (LV), and Carson City (CC).

steep rate in the weak MT middle band, and then fall almost discontinuously around 0.1 Hz where the MT fields become quite strong again due to solar wind energy. This is apparent at the Centennial Flat site, as is the case for soundings generally in the Coso area processed using these references. These non-MT artificial effects are analogous to that seen in controlled-source (CSAMT) surveys when the transmitter is too close to the survey area (Zonge and Hughes, 1991; Wannamaker, 1997).

The distortion propagates to frequencies lower than 0.1 Hz to an unknown degree so that structural images in the pertinent depth range of several km may be unreliable. Essentially only the  $xy$ -component is affected in the Coso survey, which corresponds to an  $E$ -field directed N–S ( $x$ -direction). This behavior implicates the Bonneville Power Authority (BPA) DC intertie transmission line that runs in this direction nearby to the west of the Coso field (Fig. 5), and which broadcasts electric fields roughly parallel to itself. Similar broadband non-plane wave effects due to interstate DC interties have been observed occasionally in other surveys (e.g. Wannamaker et al., 1997, 2002).

In an attempt to escape the influence of the DC intertie, remote references were tried also in Panamint Valley and Amargosa Valley, about 48 and 100 km distant from the intertie, respectively. The sounding from Panamint is shown in Fig. 6. This good-quality sounding does not show the



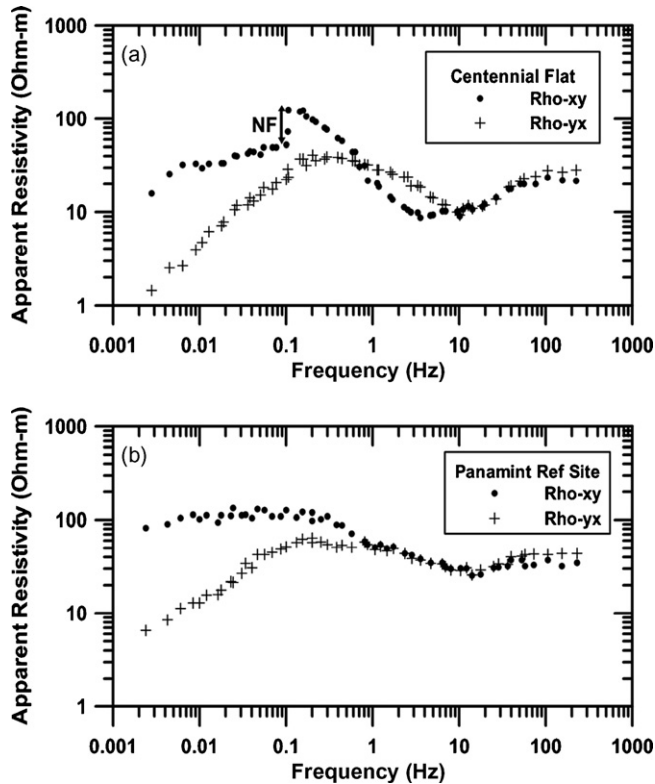


Fig. 6. (a) Apparent resistivity soundings taken at Centennial Flat about 24 km north of Coso. (b) Apparent resistivity soundings taken in eastern Panamint Valley, about 48 km northeast of the field. Note the abrupt change in Rho-xy around 0.1 Hz, indicative of a near-field (NF) or non-MT source field effect at Centennial Flat, and its absence at the more distant site (Panamint Valley). These plots were provided by the contractor (Quantec Geoscience Inc.) before final processing and band-averaging to define inversion data.

cusplike behavior near 0.1 Hz seen in Centennial Flat, and the site at Amargosa Valley was even cleaner. Initially, we concluded from this that influence of the DC intertie at these distances was minimal and that the sites would constitute sufficient references. However, other soundings in the Coso area processed using these references still showed significant cusplike behavior in this frequency range (Fig. 7, site E13 taken ~1/2 km east of well 34–9; see Fig. 1), although the results using the more distant Amargosa site were better. This was disappointing as 100 km of often winding road was reaching the limit in terms of practical, on-site reference retrieval.

It is evident that a site giving good quality plane-wave (MT) results does not necessarily serve as a good remote reference for soundings taken in a noisy environment. Clearly, EM fields which are correlated with the DC intertie are persisting at least as far away as the Amargosa Valley reference. This is occurring even though such fields have become planar by this point and only serve to improve the local MT responses at Panamint and Amargosa Valleys (e.g. see Fig. 6). The powerline fields in the Coso field area, which are quite non-planar, remain correlated in time with the Panamint and Amargosa sites and thus are not removed by remote reference processing. As emphasized by Wannamaker et al. (2004), a reference must be established which is completely outside the domain of the noise source in a survey, not just placed where the noise has become planar.

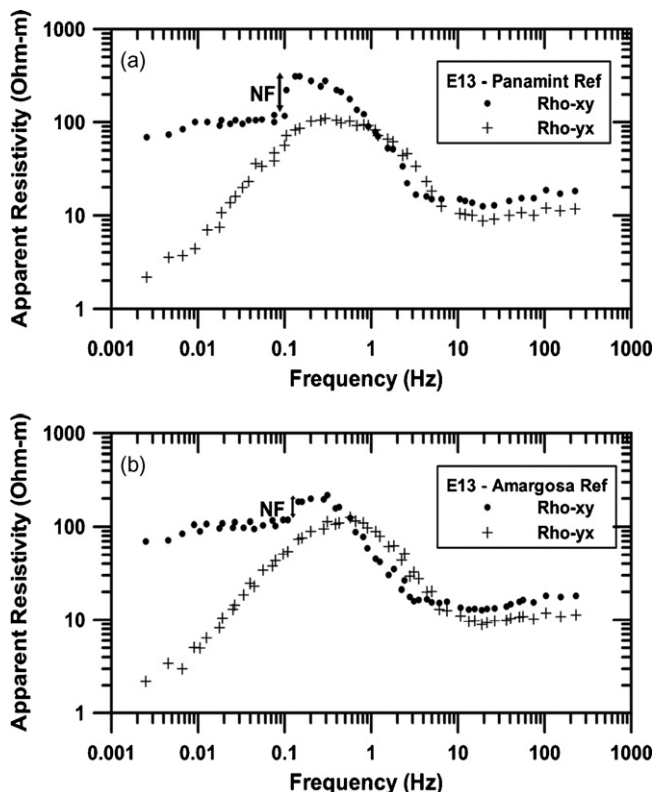


Fig. 7. Apparent resistivity data from MT Site E13 (Fig. 10) in the Coso geothermal field processed using Panamint Valley (upper) and in Amargosa Valley (lower) as remote references. Some near-field (NF) effect appears to remain near 0.1 Hz.

### 3.2. Distant remote references: Parkfield (California) observatory and Socorro (New Mexico)

More than 40 MT soundings had been taken at Coso using the various references described before the far-reaching nature of the noise source was truly recognized. To obtain high-quality results at these locations, we were faced with a complete reoccupation using a yet more distant reference, which would be expensive, or else locate a reference site of opportunity which fortuitously happened to be running while the Coso survey was underway. Such a reference site in fact exists in the way of the Parkfield, CA (PKD), permanent MT observatory, run by the University of California Berkeley Seismological Laboratory (for info, see <http://www.ncedc.org/bdsn/em.overview.html>) (Fig. 5). Due to power-law falloff and inductive dissipation of EM fields from a line-source, the DC intertie fields at PKD should be weaker than those at Amargosa by about a factor of 5, making the attempt to use PKD worthwhile. The EM time series are available at no charge essentially in real time through an ftp request. They are sampled at a rate which allows their use as a reference for frequencies up to 14 Hz, which covers the contaminated band at Coso. A plot of the results for MT Site 13 appears in Fig. 8 and indicates that the near-field effect has been corrected. The principal frequency range of distinction between the Parkfield-processed and the previous results is 1–0.1 Hz. Similarly good results were obtained for reprocessing the other about 40 sites of the Coso area.

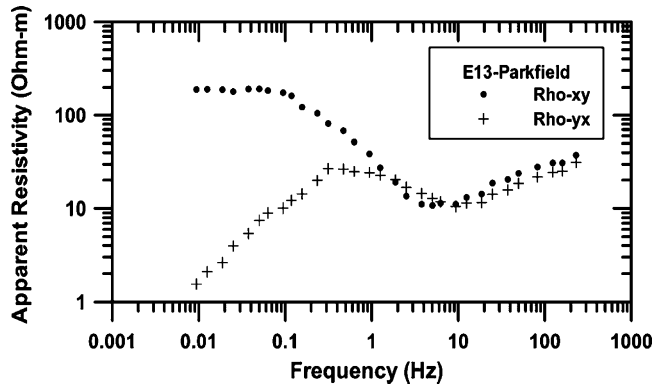


Fig. 8. Apparent resistivity data from MT Site E13 (Fig. 10) in the Coso geothermal field processed using the Parkfield MT observatory as a remote reference.

This outcome is very fortunate, but there was concern that Parkfield is barely adequate in distance and that during times of exceptionally low natural MT field activity or large powerline fluctuations there still could be some soundings whose quality would be compromised. Hence, for the remaining MT Coso soundings taken in 2003, a remote reference near Socorro, NM (SOC), more than 1000 km to the east, was used. Because it is important to recognize surveying problems as they may occur, the Coso and the reference time series should be brought together as quickly as possible. To achieve this, the field crew at Coso uploaded acquired time series to the University of Utah/EGI ftp site using the Caithness Energy high-speed computer facilities at Coso Junction, CA. The contractor's data processor/reference operator in Socorro downloaded these series from Utah using the high-speed computer facilities of the New Mexico Institute of Mining and Technology. The Coso site and reference time series thereby were combined several hours after their acquisition.

To verify that the MT time series at Socorro are well correlated with those at Coso, and Parkfield, we compare results from MT Site 29 processed with PKD with those processed using SOC (Fig. 9). The sounding curves are essentially identical indicating that Parkfield was an adequate reference in this case, although we view Socorro with more assurance as a quiet site outside the influence of the DC intertie. We considered the unusual effort of requiring the establishment of a quiet remote reference free from both local and broad-scale artificial EM interference necessary.

The fluid producing fractures at Coso are between 1 and 3 km depth (Adams et al., 2000) in plutonic rocks covered by a variable layer of hydrothermally altered overburden. This situation determines the first-order character of the soundings shown thus far, namely apparent resistivities in the 10–30  $\Omega$  m range for frequencies higher than 3–10 Hz rising to values near 100  $\Omega$  m at lower frequencies. Subtle variations in the upward slope of the apparent resistivity and the corresponding impedance-phase responses provide the second-order evidence for bedrock structure of potential geothermal significance. Thus, high-quality MT soundings are required.

Unfortunately in the second data campaign of 2005, the contractor (Apollo/Phoenix Geophysics) did not implement such a distant remote reference and the data were contaminated similarly as in our first survey before action was taken to use distant remote reference sites (Parkfield and Socorro). Nevertheless these data were judged to be of sufficient accuracy down to 0.1 Hz that they could be included in a 3D MT interpretation of the Coso area; they are useful in

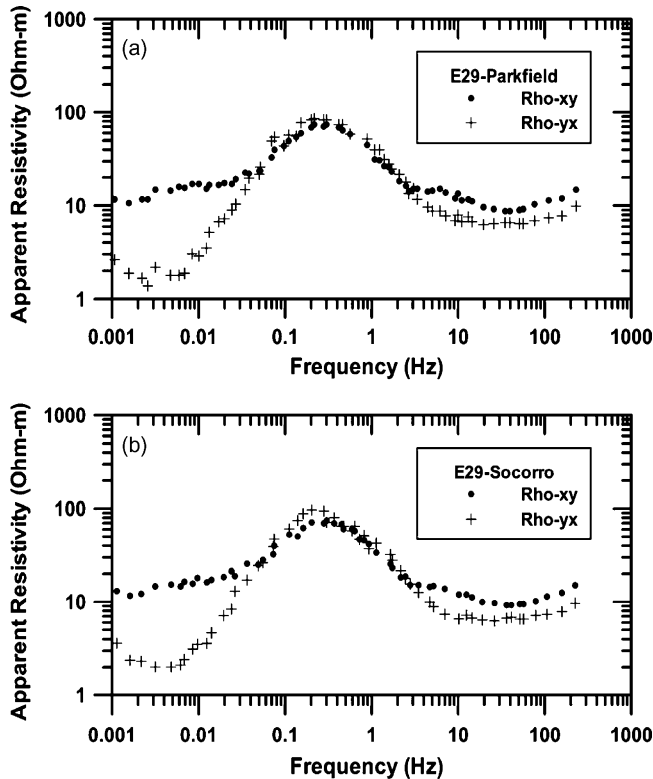


Fig. 9. (a) MT Site E29 sounding (Fig. 10) processed using the Parkfield observatory as a reference. (b) MT Site E29 sounding processed using the Socorro site as a reference.

constraining the southern boundary of the geothermal field. Because these data are not as accurate as those acquired in the first phase of the measurements, we cannot expect to extract subtle variations in the data to the same degree as with the 2003 information.

#### 4. Magnetotelluric inversion

Our ultimate aim was to construct a 3D resistivity model of the Coso geothermal field and use it to better understand its hydrothermal system by correlating it with independent geological and other geophysical information. To accomplish this goal we applied an inversion process, where the observed impedance data were fit in a least squares sense to the calculated data (i.e. the “model”). The computed data were produced by solving Maxwell’s equations for 3D resistivity variations and plane-wave source excitation at a discrete set of frequencies, which correspond to those used to specify the impedance tensor in the field measurements. To stabilize the inversion process, additional constraints were added such as spatial smoothing and bounds on the resistivity model. Because 3D MT inversion and modeling requires significant computational resources and time (Newman and Alumbaugh, 2000; Newman et al., 2003), it was more efficient to build the initial 3D resistivity model from 2D imaged sections of the reservoir. This starting model was refined subsequently through the 3D inversion process.

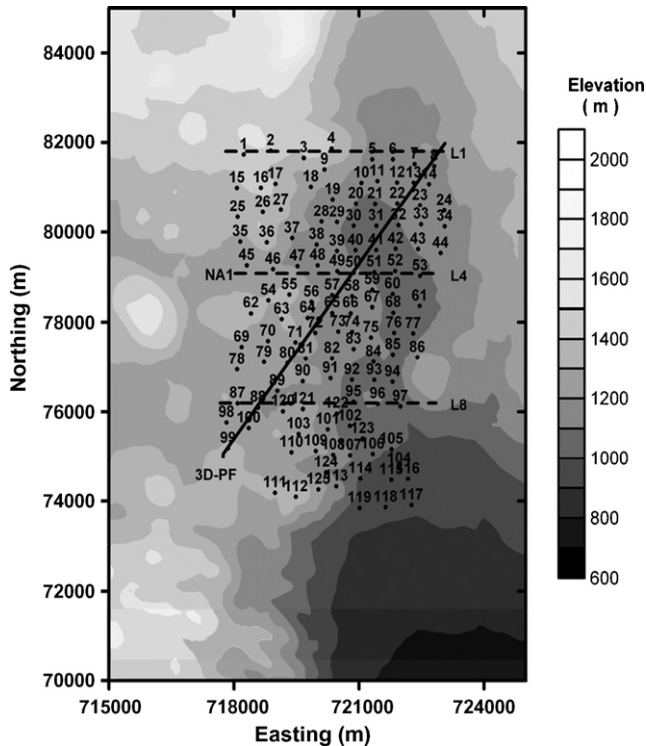


Fig. 10. Map of the Coso MT survey area; elevations given in meters above sea level. Line NA1 is contiguous to the bipole profile Navy Array 1. Sites 1–102 were acquired in 2003, and Sites 103–125 in 2005. Observed and predicted impedance data (apparent resistivity and phase) from the final 3D resistivity model will be compared along the oblique transect (3D-PF) in Fig. 18. The transect uses MT Stations 99, 100, 88, 89, 71, 72, 65, 50, 41, 32, 22, 13 and 8. Lines L1, L4, and L8 indicate the location of three of the 2D profiles used for the 3D starting model (see Fig. 13).

#### 4.1. Two-dimensional data interpretation

The initial 2D inversion was performed on relatively sparse E–W profiles of 8–10 MT sites selected from the survey map shown in Fig. 10, utilizing the 2D MT inversion algorithm of Rodi and Mackie (2001). We did not use the 2005 data in this exercise because of noise problems below 0.1 Hz due to the lack of a good remote reference. The inversions were carried out using  $Z_{yx}$  impedance data and analyzed assuming the electric field is polarized perpendicular to a presumed N–S geological strike ( $x$ -axis); in actuality, polar diagrams show that geological strike varies with frequency (i.e. it is 3D), but at the lowest frequencies (<0.1 Hz), the polarization ellipses align in a NNE direction, which follows the trend of the Basin and Range fault-block geology. In spite of the obvious limitations in modeling and inverting the Coso data in 2D, it was a logical starting point for carrying out a full 3D analysis. Here the  $Z_{yx}$  apparent resistivity and phase are defined as the transverse magnetic (TM) mode for use in the 2D inversion because 3D modeling shows that it is usually more robust than the transverse electric (TE) data to non-2D effects such as finite strike and static shifts (e.g. Wannamaker et al., 1984; Wannamaker, 1999).

Shown in Figs. 11 and 12 are 2D fits to Coso resistivity and phase data along the profile containing MT Sites 45 through 53 (L4 in Fig. 13). Fits to the apparent resistivity data (red curves) agree



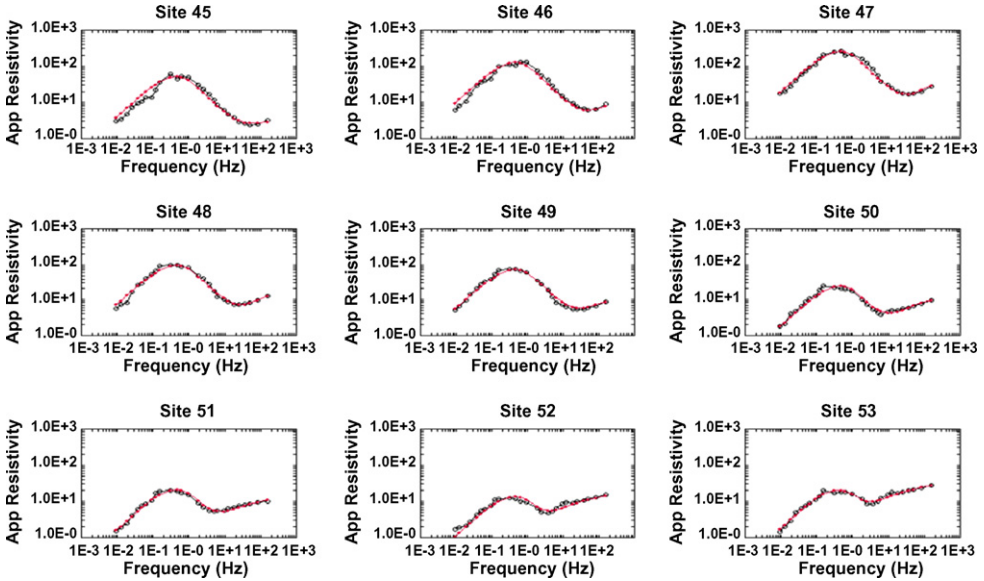


Fig. 11. Two-dimensional TM fits to the  $Z_{yx}$  apparent resistivity data, where open circles represent the field data and red curves the model responses. See Fig. 10 for site locations.

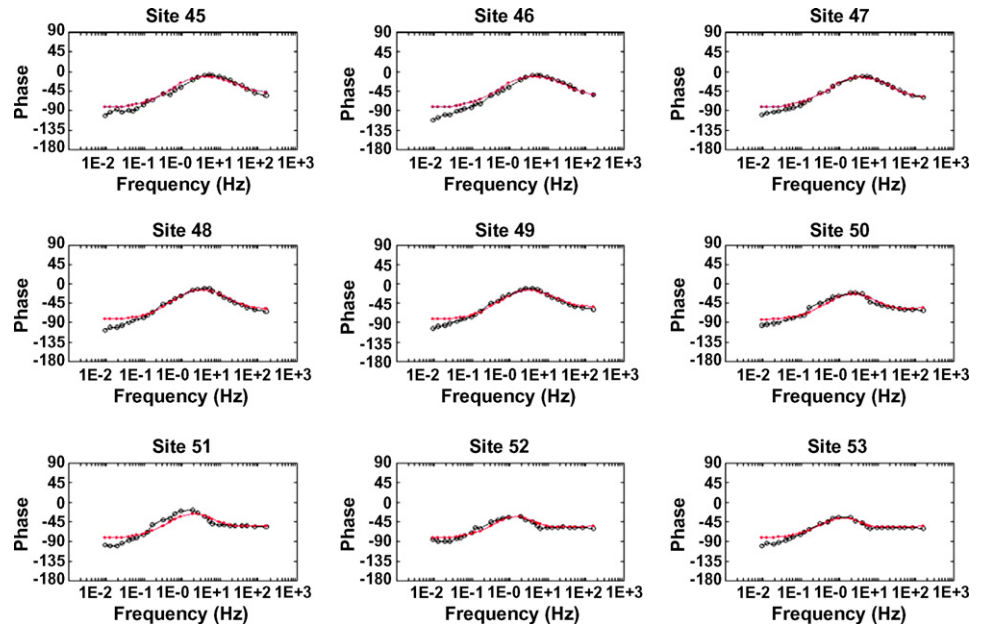


Fig. 12. Two-dimensional TM fits to the  $Z_{yx}$  impedance phase data, where open circles represent field data and red curves are model responses. See Fig. 10 for site locations.

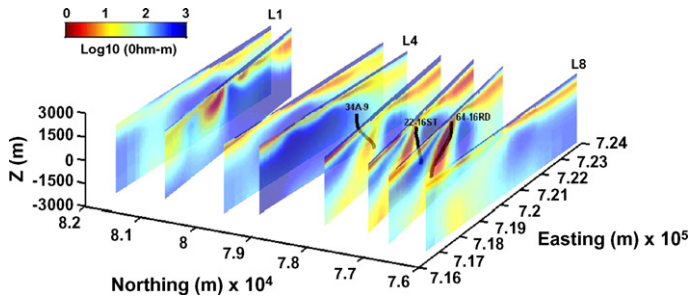


Fig. 13. Starting resistivity model of the Coso geothermal site compiled from multiple 2D transects (location of transects L1, L4 and L8 are given in Fig. 10). Traces of wells 64-16RD, 22-16ST and 34A-9 are also shown. Elevations ( $Z$ ) are given in meters above sea level.

closely with the field observations over the entire frequency band. The phase data, however, do not fit as well, especially below 0.1 Hz, most likely indicating a 3D characteristic of the data. The resulting 2D (vertical) resistivity distribution for this profile, as well as those from others, is presented in Fig. 13. Perhaps the most conspicuous feature of our ensemble of 2D inversion sections is a moderate low-resistivity zone dipping steeply west from the Coso east flank area; between Northing 79,000 and 77,000 m; this zone terminates abruptly both to the south and the north. Several of the more productive wells on the east flank dip toward this structure suggesting some correlation with higher permeability and fluid content. Wannamaker (2004) first identified this conspicuous feature using 2D TM mode analysis of the dense array Line NA1 shown on Fig. 10. The 2D inversion model of this line (Fig. 14) provides more details than individual sections of the 3D resistivity model due to the contiguous sampling over 52 bipoles, each 100 m in length. The inversion of Line NA1 also shows the west dipping lower resistivity zone seen in the sections of Fig. 13.

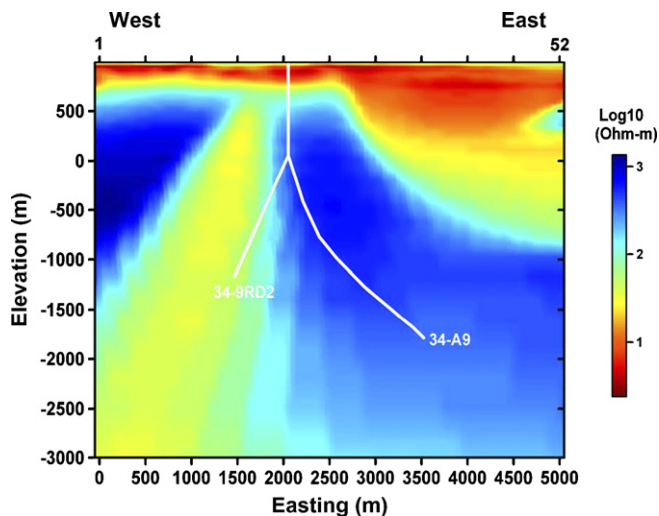


Fig. 14. Two-dimensional resistivity inversion model using TM mode data of contiguous bipole profile NA1. Also plotted are the traces of deep wells 34-9RD2 and 34-A9 that project from about 500 m south of the profile. The bottom of 34-9RD2 corresponds to a lost circulation zone. The inversion code used is based on the forward problem of Wannamaker et al. (1987) and model sensitivities of de Lugao and Wannamaker (1996).

Production well 34-9RD2 grazes the eastern boundary of this lower resistivity zone (Fig. 14). Over the bottom 350 m of the well, where it approaches the conductor most closely, a very large lost circulation zone was encountered indicating an interval with substantial open porosity (Peter Rose, personal communication, December 2006). Shallow low-resistivity material in the model represents thin alluvium and clay alteration over the eastern flank of Coso, and deeper alluvium at Coso Wash, toward the eastern part of the modeled section. Wannamaker (2004) noted that it was necessary to consider a 3D interpretational framework to fully explain all the data, not just selected modes of the data identified as TM and TE from the 2D analysis.

#### 4.2. Three-dimensional inversion of the Coso field data

The massively parallel algorithm described by Newman and Alumbaugh (2000) was used for the 3D modeling and inversion of the Coso field data, where eight 2D TM mode inversions shown in Fig. 13 were spatially interpolated to form the core of a 3D model beneath the data acquisition sites. This core model was then extended laterally over 100 km and to nearly 100 km in depth. The large area around the core model is required to satisfy the boundary conditions (scattered fields are assumed to be zero on the boundary) of the finite-difference (FD) model. The resulting 3D finite difference grid used to simulate data arising from the model, employed 244 by 258 by 120 nodes in the  $x$ ,  $y$  and  $z$  directions, respectively. The FD cells were 100-m sided cubes within the central portion of the mesh defined by the data acquisition sites. Away from the site locations the mesh cells grew in size as they approached the outer boundaries. The maximum cell dimension aspect ratio was 8 to 1, so that no dimension of a boundary cell was greater than 800 m. The interpolated 3D resistivity model provided the starting model for the 3D inversion. The simulated fields ( $Z_{xy}$  and  $Z_{yx}$  apparent resistivity and phase) for this starting model are shown in Figs. 15 and 16 and are compared with the corresponding field observations for Sites 45 through 53.

For frequencies above 1 Hz, the 3D fields generally show good correspondence with the measured data for both polarizations, even though there are some grid-induced statics arising from the interpolation process that affect primarily the predicted  $Z_{xy}$  apparent resistivity at a few sites. It is expected that the  $Z_{xy}$  data would show the poorest fit to the 3D model because it is constructed of 2D sections generated by fitting the  $Z_{yx}$  data. Significant differences, however, arise at all sites between the model and field curves in both apparent resistivity and phase at lower frequencies. When the field data were analyzed using 2D assumptions, such discrepancies were most apparent in the phase data.

While all the complex impedance tensor elements can be considered as data in the inversion, it was found that the on-diagonal terms ( $Z_{xx}$ ,  $Z_{yy}$ ), which have much lower magnitude, and thus lower signal-to-noise, than the off-diagonal terms ( $Z_{xy}$ ,  $Z_{yx}$ ), generally degraded the performance of the inversion. Thus, we included only the off-diagonal elements. Also designing a FD mesh that will accurately represent the electromagnetic fields over the entire frequency range in the inversion of the observed data can be quite challenging. Practical considerations required that the entire frequency range of the data was not to be fitted simultaneously at first, but in three phases.

In the solutions presented here we first restricted the 2003 data over the 250–1 Hz frequency range utilizing a mesh with 120 nodes along each coordinate direction that spanned distances of 120 km in the horizontal dimensions to satisfy boundary conditions. The mesh also extended 30 km into the air and 60 km into the Earth. The smaller mesh utilized for this frequency range allowed for fast processing times and the model obtained was used as a starting model in the next phase of the image processing. In the second phase we added 2003 data down to 0.3 Hz, and in the final and third phase we added the data acquired in the 2005 campaign (250–0.3 Hz). To accommodate

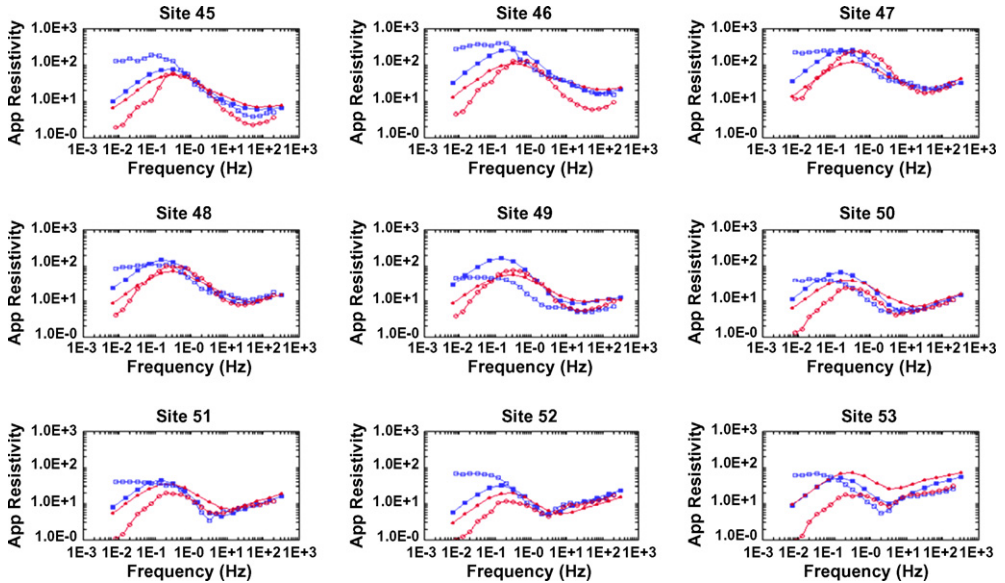


Fig. 15. Comparison of apparent resistivities for Sites 45–53 that were based on the initial 3D starting model generated from the interpolated 2D TM mode inversion. The blue curves with solid and open squares denote predicted and observed  $Z_{xy}$  apparent resistivities, respectively. The red curves, solid and open circles, denote predicted and observed  $Z_{yx}$  apparent resistivities, respectively.

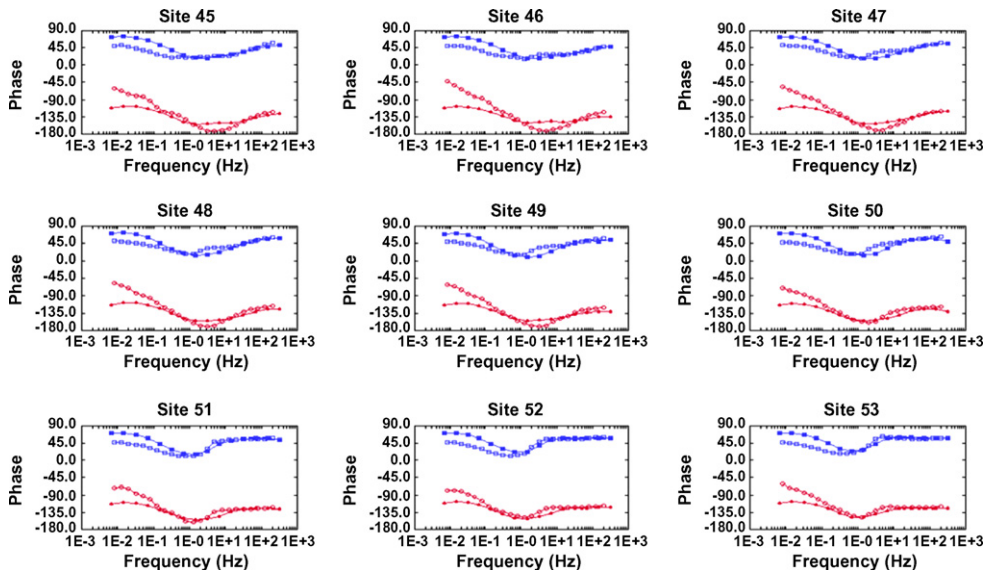


Fig. 16. Comparison of impedance phases for Sites 45–53 that were based on the initial 3D starting model generated from the interpolated 2D TM mode inversion. The blue curves with solid and open squares denote predicted and observed  $Z_{xy}$  phases, respectively. The red curves, solid and open circles, denote predicted and observed  $Z_{yx}$  phases, respectively.

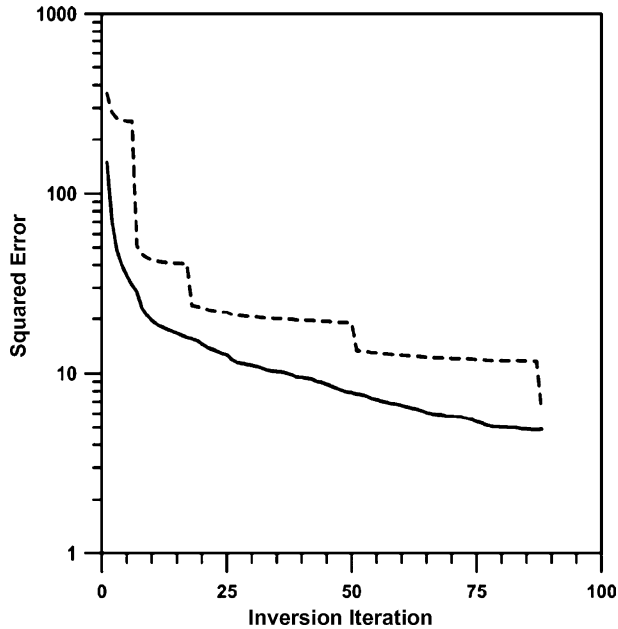


Fig. 17. Plot of the convergence of the 3D inversion iteration for the 100–1 Hz data. The dashed curve is a plot of the convergence of the error functional with the regularization constraint. The solid curve is a plot of the data misfit (weighted squared error) without the regularization penalty term.

the lower frequency data in phase two and three of the image processing, we expanded the mesh to 244, 258 and 120 nodes along each coordinate in order to move its boundaries out a sufficient distant to insure quality results. The accuracy of these two meshes were tested and verified to within a few percent based on 1D forward models over the two frequency ranges, and were shown to have depth sensitivity to 5 and 15 km, respectively. This should be adequate for mapping the depths of interest in the geothermal system.

Out of the 102 MT stations acquired in 2003 over the east flank of the Coso field, only one station was discarded because of severe noise problems; we also disregarded data from six stations of the 2005 survey. In the inversion processing we assumed a 5% noise floor, based upon the amplitude of each impedance measurement, where the data were weighted by the noise estimates.

The first 3D inversion analysis (250–1 Hz data) was carried out at the National Energy Research Scientific Computing Center (NERSC) of Lawrence Berkeley National Laboratory, where 512 IBM SP2 processors were employed. On this platform for a 48-h period, 15 inversion iterations could be completed on average. Shown in Fig. 17, is a plot of the convergence of the inversion iteration. The dashed curve is a plot of the convergence of the error functional with the regularization constraint. The step-like features in this graph correspond to reducing the level of smoothing in the inversion process as the iteration proceeded. The solid curve is a plot of the weighted squared error, the data misfit without regularization. While we did not achieve the target data misfit of one, we observed a good reduction in the weighted squared error from 149 to 4.8 at the 88th inversion iteration.

Subsequent analysis using the lower frequency data was carried out on a more powerful Infini-band Linux cluster utilizing 100 processors; for the same number of processors the Linux cluster is about 3–5 times faster than the NERSC platform. With the 2003 augmented data we were able



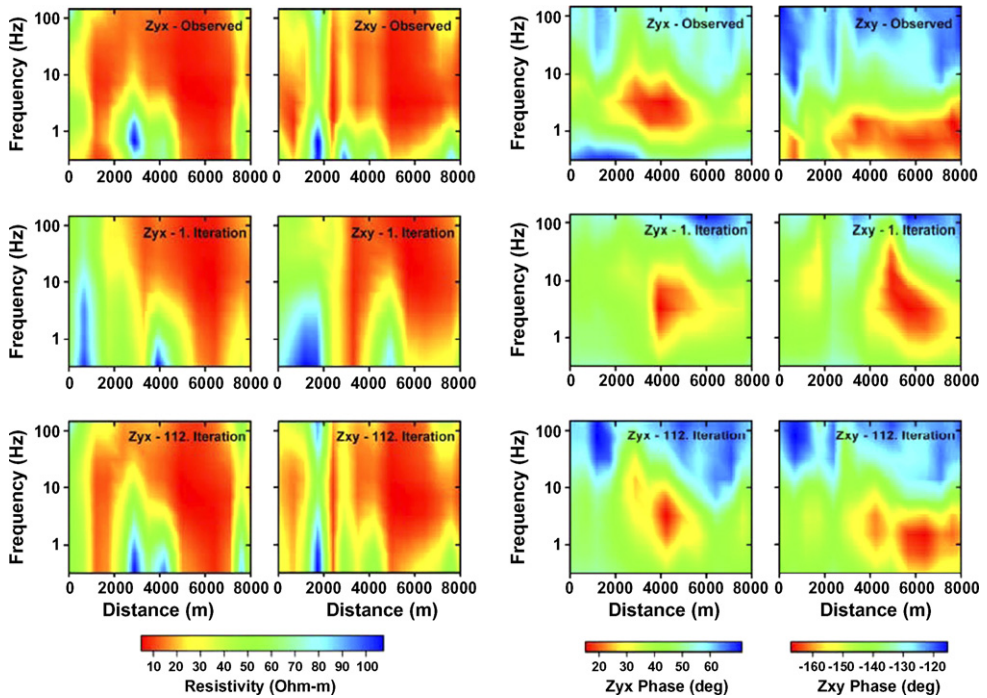


Fig. 18. Pseudo-section plots of  $Z_{yx}$  and  $Z_{xy}$  apparent resistivities and phases for observed and predicted data along the transect 3D-PF indicated in Fig. 10. The predicted data arise from the final 3D resistivity model given in Fig. 19. Horizontal offsets in these plots are relative to Site 99. Predicted results are shown for the first and final inversion iterations showing the improvement obtained in the data fit.

to reduce the data misfit to 2.99, which is still a factor of three above the desired noise threshold. When we added the 2005 data the final misfit was 3.2. Closer inspection of the data fits indicates the inability to fit the data to the assumed noise threshold appears to arise from noise in the MT 3–0.3 Hz deadband, which also appears to affect the 2005 data more than those of the 2003 campaign; this should come as no surprise given the use of a “local” remote reference in the 2005 survey. Nevertheless the predicted data produced from the resistivity model based on both the 2003 and 2005 data sets showed good improvement when compared to those generated by the starting model (Fig. 18).

#### 4.3. The three-dimensional resistivity model

The final 3D resistivity inversion model is illustrated in Fig. 19. The most obvious feature is the red core of low resistivity centered within well production and reinjection intervals along with micro-earthquake (MEQ) locations. Most of the MEQ events are related to volumes changes arising from commercial exploitation of the reservoir (Julian et al., 2004). The event locations also appear to correlate with transition boundaries in the resistivity to some degree; we will have more to say about this later.

A horizontal depth slice from the final model at an elevation of 500 m below sea level in Fig. 19 is given in Fig. 20. The most prominent feature in this figure is the low-resistivity central region. The mapped surface expressions of right-lateral faults running S–N in the figure bound this

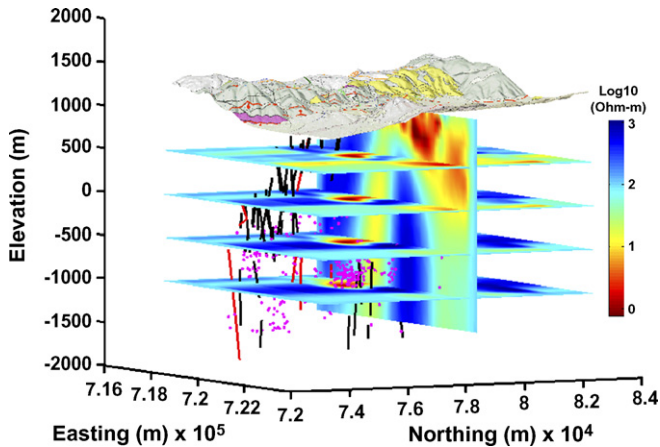


Fig. 19. Three-dimensional 3D resistivity image derived from Coso MT data sets. Black and red linear segments denote well production and reinjection intervals. The red dots correspond to micro-earthquake focus locations. Elevations given in meters above sea level.

region to the NE and SW, implying the faulting is nearly vertical to 1000 m depth. This region also exhibits temperatures above 250 °C, high permeability and contains large amount of fluids. On the other hand, the area around MT Sites 87, 88, 98, 99, and 100 has similarly high temperatures and significant geothermal fluid production from 2 to 3 km depth, but shows only moderate, and a non-descriptive resistivity structure of approximately 50  $\Omega$  m; we shall discuss the implications of this finding in more detail later on. This zone is also clearly bounded by NE–SW and NW–SE trending faults that define the productive area of the field and appear to act as hydrological barriers.

Because the low-resistivity structure is such a conspicuous feature in the 3D resistivity model, which persists from the prior starting model, a sensitivity test was carried out where the structure was replaced by the more resistive material on its flanks. The resulting data misfit was 35% greater than what was observed for the final misfit with the low-resistivity structure, indicating its importance in the model. Furthermore, two other independent observations confirm this assessment. As we already mentioned, fault traces in Fig. 20 clearly mark the NE and SW boundaries of the structure. More convincingly we shall present below the 3D seismic velocity model of Coso of Lees and Wu (2000) developed based on MEQ data that shows a stunning correlation with the low-resistivity structure in Fig. 20.

A vertical (W–E) section at Northing 81,000 m (PF1 in Fig. 20) is given in Fig. 21. In the eastern part of this section, the resistivity structures dip to the east and implies that in this area the thickness of the sediments in the Coso Wash graben is less than about 1000 m. The two unnamed normal faults depicted in Fig. 20 as “2” and “3” and the Coso Wash fault “1” correlate with the easterly dipping resistivity structures; the sediment thickness in the downthrown blocks of these faults increase to about 2000 m. To the west, subvertical contacts between low- and high-resistivity materials are evident.

Fig. 22 shows a vertical (W–E) section at Northing 79,900 m that intersects the Coso Hot Springs (PF2 in Fig. 20), which are located directly above a high-resistivity feature on the easterly dipping contact between the central resistor and the more conductive valley fill to the east. Note that the area around and north of Coso Hot Springs is a protected historical site; hence no drilling is allowed in this part of the geothermal field.

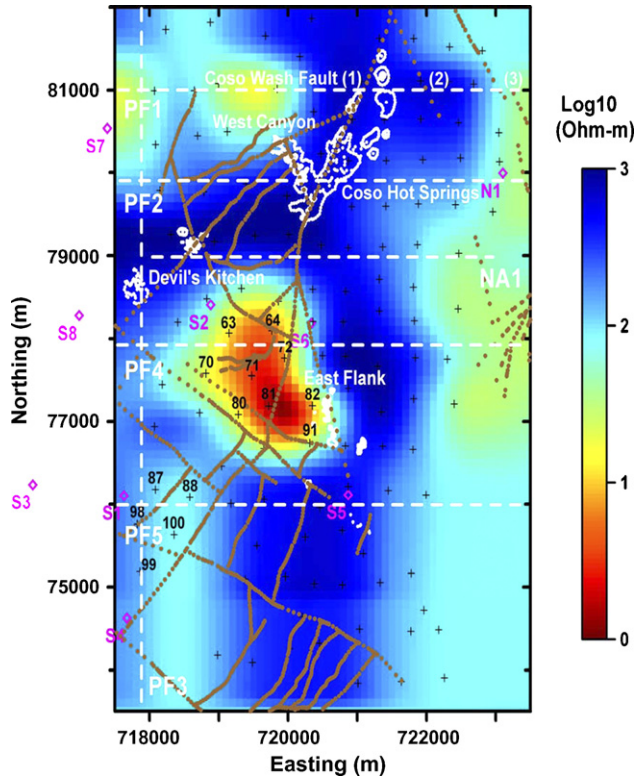


Fig. 20. Horizontal slice through the 3D resistivity model at 500 m below sea level; average ground surface elevation is 1200 m above sea level. Geothermal surface manifestations areas are outlined in white. Mapped surface fault expressions are shown by the brown lines (dotted were inferred); (1) correspond to the Coso Wash Fault, while (2) and (3) to two unnamed faults. Micro-earthquake seismic stations (S1, S2, S3, S4, S5, S6, S7 and N1) from Lees and Wu (2000) are shown in purple. MT sites are indicated by the black crosses. White dashed lines (PF1, PF2, NA1, PF3, PF4 and PF5) correspond to the location of the vertical cross-sections of the final model shown in Figs. 21–25 and 27, respectively.

Fig. 23a is a vertical section corresponding to the 2D resistivity section along the high-density MT line of Wannamaker (2004) (NA1 in Fig. 20) shown in Fig. 14. The vertical section through the 3D model at a location 700 m to the south is shown in Fig. 23b for comparison. The 2D inversion in Fig. 14 appears to be responding to the resistivity structure given in Fig. 23b. In other words, the vertical section in Fig. 23b is much closer to the 2D inverted result than is the section directly beneath the 2D line. The 2D and 3D inversion sections to first-order imply that the dipping conductor becomes much more pronounced to the south of the dense array line (Line NA1).

The 3D inversion sections overall are expected to be a more accurate representation of structure directly beneath them since an attempt was made to fit both impedance polarizations of all profiles, simultaneously. However, we do not believe the conductor imaged under Line NA1 is entirely due to sideswipe from the lower resistivity found 500 m or more to the south. This is because the 2D image in Fig. 14 is only 200–300 m wide where it comes near the surface. We conclude there must be a vestige of the dipping conductor under or very close to Line NA1, but the advantage of 3D coverage is that the maximal expression of the conductor can be pinpointed with more confidence.

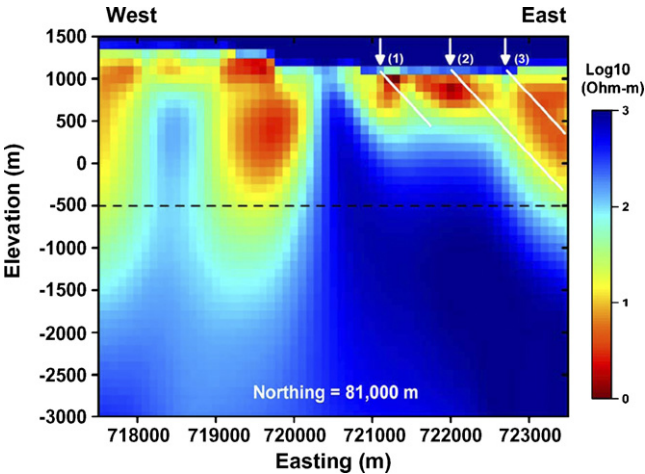


Fig. 21. Vertical (west to east) resistivity cross-section PF1 at Northing 81,000 m. The fault marked (1) is the Coso Wash Fault, faults (2) and (3) are unnamed and shown in plan view in Fig. 20. The horizontal black dashed line corresponds to the elevation of the horizontal slice shown in Fig. 20. The resistivity in the air region was set at  $10^{10} \Omega \text{ m}$ , but is indicated at the top of the section by a dark blue strip ( $10^3 \Omega \text{ m}$ ) on the color scale to compress the resistivity range and better render the resistivity variations within the Earth.

An S–N transect (PF3 in Fig. 20) that intersects the Devil’s Kitchen structure is shown in Fig. 24. As with the resistivity structure beneath the Coso Hot Springs, Devil’s Kitchen is over a high-resistivity feature at depth. Its location coincides with the surface termination of a high–low-resistivity contact that would suggest a fault that in Fig. 24 dips to the north from Devils’ Kitchen.

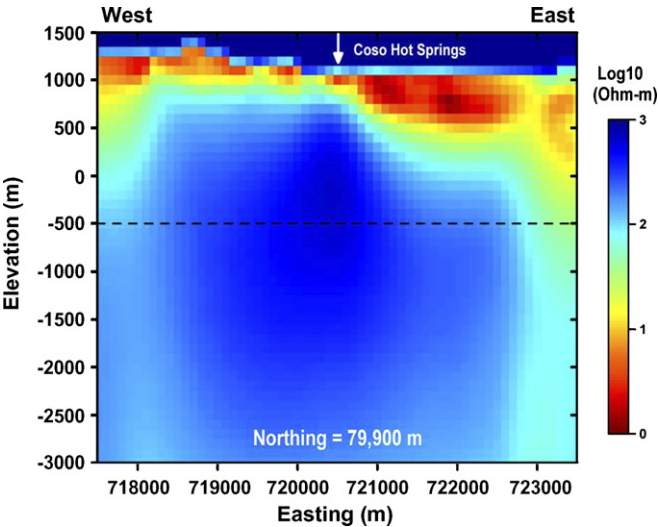


Fig. 22. Vertical (west to east) resistivity cross-section PF2 at Northing 79,900 m. The section intersects Coso Hot Springs at the location shown by white arrow. The horizontal black dashed line corresponds to the elevation of the horizontal slice shown in Fig. 20. The resistivity in the air region was set at  $10^{10} \Omega \text{ m}$ , but is indicated at the top of the section by a dark blue strip ( $10^3 \Omega \text{ m}$ ); see caption of Fig. 21.

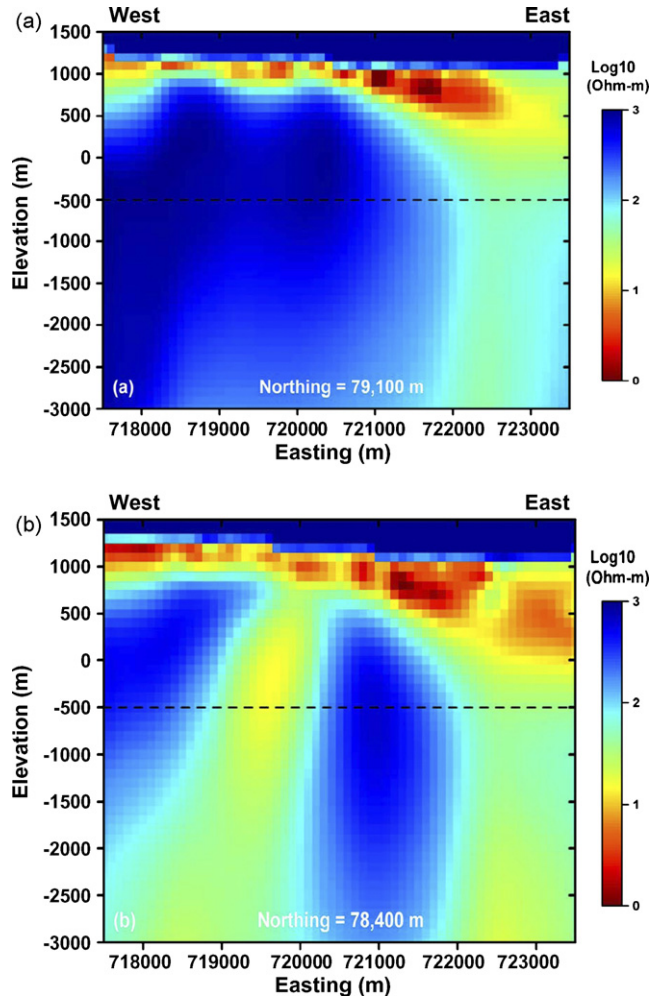


Fig. 23. (a) Vertical (west to east) resistivity cross-section at Northing 79,100 m which is the location of the high-density MT line (Line NA1) used to generate the 2D resistivity section shown in Fig. 14. (b) Vertical (west to east) cross-section at Northing 78,400 m. The horizontal black dashed lines correspond to the elevation of the horizontal slice shown in Fig. 20. The resistivity in the air region was set at  $10^{10} \Omega \text{ m}$ , but is indicated at the top of the section by a dark blue strip ( $10^3 \Omega \text{ m}$ ); see caption of Fig. 21.

This is an area exhibiting subsurface temperatures above  $250^\circ\text{C}$  and crustal thinning that exemplifies the Coso reservoir as a whole (Monastero et al., 2005), where the brittle–ductile transition zone is at about 4 km depth.

High resistivity in the Devils' Kitchen area corresponds with many of the production well intervals and is interpreted as a resistive propylitic alteration zone within the reservoir; we will have more to say about this shortly. There are two low-resistivity zones—a shallow one that has lateral continuity, and a deeper one that is possibly related to the brittle–ductile transition. The PF3 transect also intersects an area of high geothermal well density, where the near surface low resistivity is interpreted as a clay cap alteration zone caused by the geothermal fluids beneath.



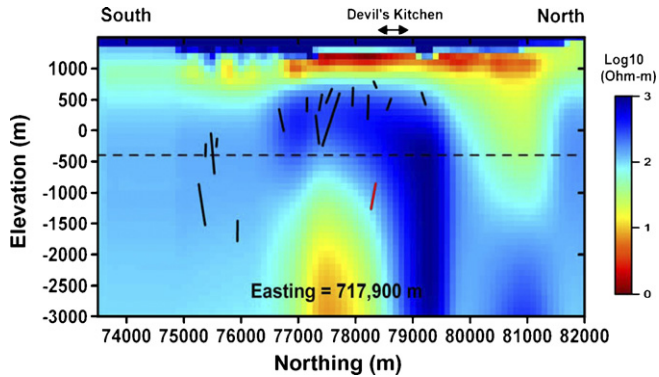


Fig. 24. Vertical (south to north) resistivity section PF3 at Easting 717,900 m that runs through the Devil's Kitchen area. Black and red lines indicate producing and injection well intervals, respectively. The horizontal black dashed line corresponds to the elevation of the horizontal slice shown in Fig. 20. The resistivity in the air region was set at  $10^{10} \Omega \text{ m}$ , but is indicated at the top of the section by a dark blue strip ( $10^3 \Omega \text{ m}$ ); see caption of Fig. 21.

The producing intervals of all the wells between Easting 717,400 and 717,900 m are shown as nearly vertical black lines in Fig. 24; a single injection interval is shown as a red vertical line. This figure illustrates two general observations about the correlation between well production zones and the resistivity structure, (1) to the north of Northing 76,000 m the producing intervals are located in high-resistivity material below the low- and high-resistivity transition zone, and (2) in the SW area of our survey (south of Northing 76,000 m) there is an area of intermediate resistivity ( $\sim 50 \Omega \text{ m}$ ) with no sharp resistivity contrasts where many successful production intervals are found.

The perpendicular transect at Northing 76,000 m through the SW area of our survey (PF5 in Fig. 20) is presented in Fig. 25. Here again a conductive cap is observed overlying the more resistive reservoir rocks; it has already been illustrated that fluid production in the southwest sector of the Coso field appears to be controlled by the fault geometry shown in Fig. 20. Further observation along the Devil's Kitchen transect (Fig. 24) suggests that the deformation caused by igneous intrusions has produced significant fracturing. The boundaries between the older and younger rocks are represented by the transitions between low- and high-resistivity regions. We believe the fracturing at the boundaries provides good permeability for geothermal fluid production.

The images in Figs. 22 and 24 show a well-established pattern when MT is used to map geothermal resources in high-temperature ( $>230^\circ \text{C}$ ) environments, which is clearly the case at Coso. The conceptual model consists of a conductive argillic (smectite clay) hydrothermal alteration zone above and adjacent to more resistive illite clays that formed from propylitic alteration within the geothermal reservoir (Anderson et al., 2000; Cumming et al., 2000; Ussher et al., 2000); matrix conductivity within the reservoir is influenced much more by the resistive illite clays, than the fluid-filled fractures.

Lutz et al. (1996) has documented the clay mineralogy at Coso along the Devil's Kitchen transect (Fig. 24), which varies systematically with temperature and depth. Three hydrothermal alteration zones were recognized: the smectite, illite–smectite and illite zones. The smectite and mixed smectite–illite zones were reported to thicken from north to south. The illite zone, the deepest one, contains illite, chlorite, epidote and wairakite. These authors also reported that the depth of illite zone increased from 750 m depth from the surface, in the vicinity of the Devil's Kitchen area, to depths greater than 1200 m to the south. This is consistent with the depth where increased resistivity is observed and corresponds to the shallowest part of the producing inter-

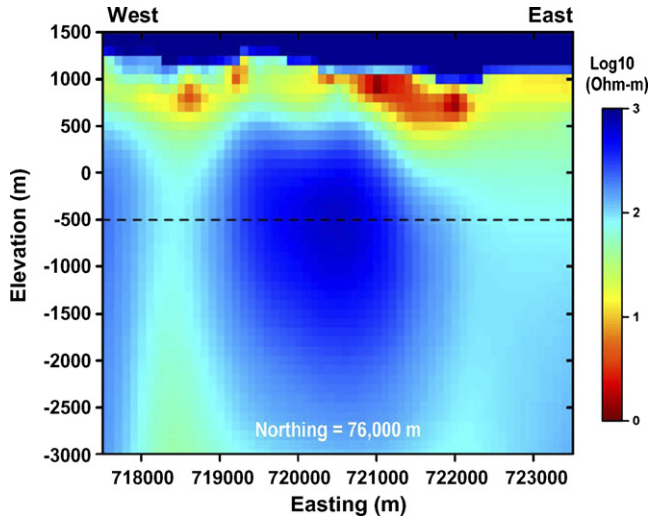


Fig. 25. Vertical (west to east) resistivity cross-section PF5 at Northing 76,000 m. This section intersects a region with a large number of geothermal well feed zones between Easting 717,400 and 719,000 m. The horizontal black dashed line corresponds to the elevation of the horizontal slice shown in Fig. 20. The resistivity in the air region was set at  $10^{10} \Omega \text{ m}$ , but is indicated at the top of the section by a dark blue strip ( $10^3 \Omega \text{ m}$ ); see caption of Fig. 21.

vals in Fig. 24. The temperature observed with this change in clay mineralogy corresponds to approximately  $230^\circ\text{C}$ .

The shape of the subsurface resistivity structure in Figs. 22 and 24, best exemplifies the anomaly of choice for delineating high-temperature geothermal reservoirs; a conductive clay cap diagnostic of the underlying reservoir that also shows an apex in the base of the argillic–smectite clay cap beneath a fumarole area (e.g. Coso Hot Springs and Devil’s Kitchen). A case could be made in applying this conceptual model to the resistivity section in Figs. 21 and 23a, and Fig. 25 as well, but the resistivity section in Fig. 23b is too complex to be easily described by this model.

#### 4.4. The geophysical signature

Electrical resistivity and seismic velocity depend on many physical conditions. Within the complexity of a geothermal system it is difficult to isolate unique relationships that allow an unambiguous interpretation of inferred geophysical parameters such as electrical resistivity, acoustic and shear velocity. Just as the physical properties, mineral composition, fracturing, fluid saturation, temperature, porosity and pressure, affect the geothermal characteristics of the subsurface, they also influence the geophysical parameters that can be inferred from the surface. In this study we investigated first-order correlations between seismic and electrical geophysical structure and suggest causative mechanisms for anomalous regions.

Electrical resistivity is primarily a function of water/brine saturation, porosity and the electrical resistivity of the fluid filling the pore space (Palacky, 1987). In fractured media, porosity and permeability are dominated by that of the fractures. The electrical resistivity of the pore water is controlled mainly by salinity and less so by temperature. The mineral composition of the rocks, particularly the amount and type of clays present, also has a first-order effect on the bulk electrical resistivity of the rock mass.

For rock of relatively uniform composition both acoustic and shear velocity decrease with increasing temperature (Christensen, 1989). Acoustic velocity ( $V_p$ ) tends to decrease faster with temperature than shear velocity ( $V_s$ ) resulting in a decrease in the  $V_p/V_s$  ratio as temperature increases. However, the situation is more complicated in the Earth, where  $V_p/V_s$  ratio is observed to increase with temperature and fracture density (Sanders et al., 1995). Rocks with randomly oriented fractures have smaller seismic velocities compared to those of unfractured rocks. Since  $V_p$  decreases less than  $V_s$  as the density of fractures increases, generally  $V_p/V_s$  is higher when rock fracture density is greater (Schön, 1996). Acoustic velocity generally increases with fluid saturation, while shear velocity is only slightly affected by the change in density.

#### 4.5. The MT resistivity and MEQ velocity models and their interpretation

A synthesis of much of the previous geochemical and geophysical work at Coso is given by Lees and Wu (2000). They present an intrusive model for Coso that places a magmatic body at depths greater than 5 km below the triangle formed by micro-earthquake (MEQ) Stations S1–S3–S4 and propose the following model. The center of magma movement is close to the S1–S3–S4 triangle (just to the SW of our MT survey area shown in Fig. 26). Hot magma arose from depth and spread out in all directions. It flowed due north and east following the two pre-existing sets of faults.

The 3D seismic velocity model derived from tomographic inversion of MEQ data (Wu and Lees, 1999; Lees and Wu, 2000) was provided to us for comparison with the 3D MT resistivity model. The tomographic model used a cell size of 200 m by 500 m in the horizontal and vertical directions, respectively. The MEQ inversions produced models of acoustic and shear velocities, and the associated  $V_p/V_s$  ratios.

Examination of the 3D velocity and 3D resistivity models shows many interesting correlations. Fig. 26 depicts the  $V_p/V_s$  distribution at 500 m below sea level and the same surface features and markers used in Fig. 20. Black dashed lines indicate locations of vertical cross-sections PF1–PF5 and NA1. The correlation between the high  $V_p/V_s$  and low resistivity in the central portion of the two figures (between Easting 718,500 and 720,500 m, and Northing 77,000 and 78,500 m) is striking. The high  $V_p/V_s$  and low electrical resistivity region is bounded by two sets of mapped faults. The area of low  $V_p$  and  $V_s$ , and high  $V_p/V_s$ , is interpreted by Lees and Wu (2000) as probably being fluid-saturated. This is consistent with low electrical resistivity. Besides fracture density, Sanders et al. (1995) also point out that increases in  $V_p/V_s$  ratio are related to increases in temperature and partial melt. While at Coso there is no partial melt at reservoir depths, the reported high temperatures (exceeding 250 °C) in this area may further enhance the  $V_p/V_s$  ratio. To the north the low  $V_p/V_s$  and high resistivity both align with the surface expression of the Coso Wash Fault.

In the southwestern corner of the MT survey (MT Stations 87, 88, 96, 99 and 100), where one finds the anomalous ring structure in the  $V_p/V_s$  ratio (Fig. 26) and the intermediate electrical resistivity on the order of 50  $\Omega$  m (Fig. 20), there is significant geothermal fluid production from 2–3 km depth. Whereas the  $V_p/V_s$  ratio map provides a clear indication of production intervals in the SW portion of the survey area, the electrical resistivity gives only a slight indication. This lack of correlation between the  $V_p/V_s$  and resistivity structure in this region may be attributed to the truncation of the MT survey data and/or its lack of sensitivity to the producing fluid intervals. We have no data to the south and west of the SW corner area and believe that better correlations could be obtained if the MT data could be acquired there. Northeast of that corner we find a NW-trending band of high electrical resistivity and low  $V_p/V_s$  ratio.

North and east of Devil's Kitchen there is a SW-trending zone of low  $V_p/V_s$  and high electrical resistivity that generally aligns with the surface expression of the Coso Wash Fault. This feature

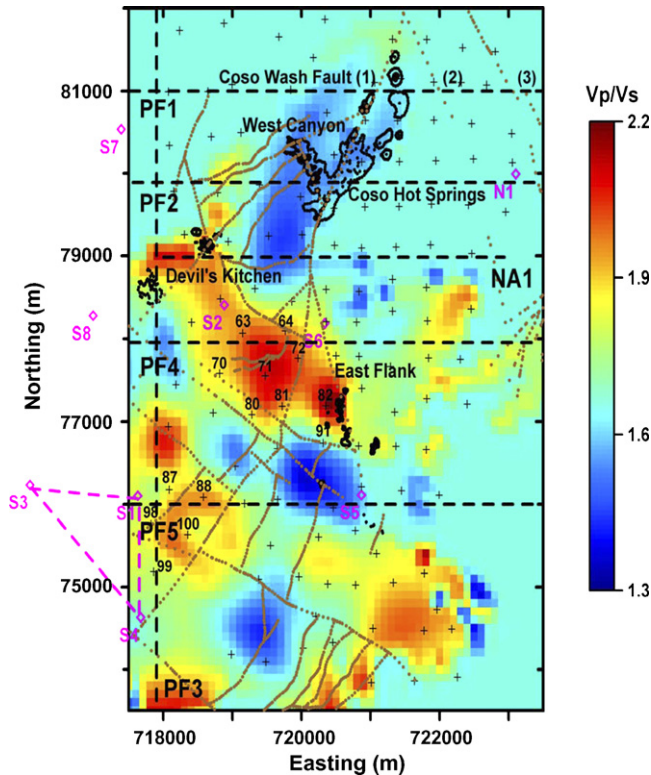


Fig. 26. Horizontal slice through the 3D seismic velocity model derived by Lees and Wu (2000) on the basis of micro-earthquake (MEQ) data at 500 m below sea level; average ground surface elevation is 1200 m above sea level. Geothermal surface manifestations areas are outlined in black. MEQ seismometer locations (S1, S2, S3, S4, S5, S6, S7, S8 and N1) used for velocity tomography are indicated in purple. Mapped surface fault expressions are shown by the brown lines (dotted were inferred). Black dashed lines (PF1, PF2, PF3, PF4, PF5 and NA1) correspond to the locations of the cross-sections presented in Figs. 21–25 and 27.

is seen in the center of Fig. 21 with nearly vertical boundaries between low- and high-resistivity areas to the west and an easterly dipping contacts to the east.

There is a distinct difference between the SW area in Figs. 20 and 26 where high  $V_p/V_s$  correlates with moderate electrical resistivity ( $\sim 50 \Omega \text{ m}$ ) and the area to the NE (MT Stations 63, 64, 70, 71, 72, 80, 81, 82 and 91) where high  $V_p/V_s$  correlates with low electrical resistivity ( $\sim 0.75 \Omega \text{ m}$ ). Recent wells on the eastern flank of this latter structure that were drilled into the transition zone between the low- and high-resistivity regions encountered large open fractures that resulted in large drilling mud losses (Fig. 27) (Frank Monastero, personal communication, December 2005) indicating that there the formation fluids were under-pressured. The presence of these fractures along the flanks of the low-resistivity region, plus the high  $V_p/V_s$  feature suggests that this is an area that is highly fractured and that fluids are nearby. Another intriguing possibility, given the reported high temperatures in and around this structure, is that the low resistivity could have arisen from the boiling of formation fluids, where the remnant fluid exhibits increased salinities. However, fluids encountered in and around this area so far do not show any enhanced salinity compared to fluids drawn from the western part of the field (Frank Monastero, personal communication, December 2007). Finally, it is important to note that the depth to the brittle–ductile transition

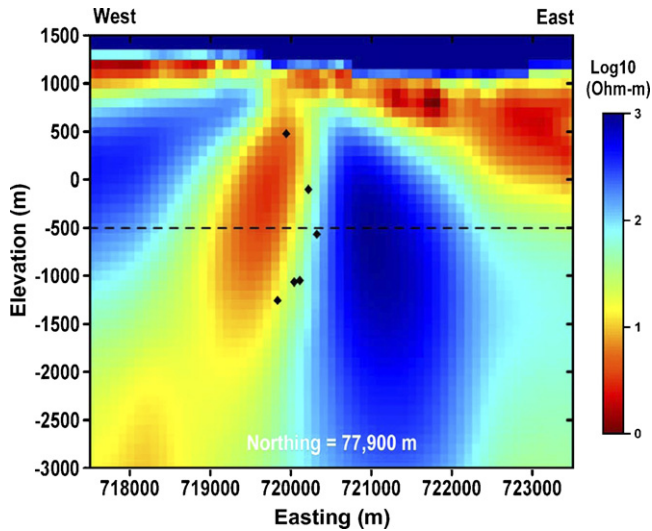


Fig. 27. Vertical (west to east) resistivity cross-section PF4 at Northing 77,900 m. The locations of zones major drilling mud losses (i.e. large open fractures) are shown by the black solid diamonds. All mud-loss locations are within 800 m to the north of the section and are in the transition zone between high- and low-resistivity regions. The horizontal black dashed line corresponds to the elevation of the horizontal slice shown in Fig. 20. The resistivity in the air region was set at  $10^{10} \Omega \text{ m}$ , but is indicated at the top of the section by a dark blue strip ( $10^3 \Omega \text{ m}$ ); see caption of Fig. 21.

zone is shallowest here (i.e. at 3.5 km depth) and the area exhibits maximum crustal thinning (Monastero et al., 2005).

## 5. Conclusions

High-quality broadband MT data were acquired in the Coso geothermal field following efforts to establish an adequately distant, clean remote reference. It is not sufficient to use a reference site that appears to give good plane-wave results local to the reference. This is because there may be EM noise fields (albeit planar) at the reference site that are correlated in time with those of the survey area, which are non-planar in geometry. In the 2003 survey, we found that MT time series at the permanent Parkfield observatory in California were adequate as reference fields to the sites at Coso. In the course of doing this, technology has been established to generally utilize the Parkfield data in MT surveying, thereby improving survey quality for other applications. Noise sources of scales as broad as that of the BPA DC intertie are rare, but this particular one may be a factor in exploration of numerous other geothermal systems in western Nevada and easternmost California due to its proximity.

A 3D resistivity model of the Coso geothermal field was developed using full 3D inversion of 125 MT sites over a frequency band of 250–0.3 Hz. In order to produce a geologically meaningful results the starting model was constructed from a series of 2D resistivity images along E–W transects, approximately perpendicular to the regional geological strike. The 2D inversions were carried out using  $Z_{yx}$  impedance data and analyzed assuming the electric field is polarized perpendicular to a presumed N–S geological strike. We employed this strategy to save time and a good starting model that could be better refined in the inversion process. The 3D resistivity model that was developed clearly confirms that faulting strongly controls the geological structure, as well as geothermal fluid production at Coso. These faults act as hydrological barriers to

fluid flow, compartmentalizing zones where fluids can be exploited, and in some instances have been targeted by drilling into them from the east flank of the field. Several transects through the 3D resistivity model show the classic MT response of a high-temperature geothermal reservoir, exemplified by Coso, which presents a conductive argillic (smectite clay) hydrothermal alteration zone that sits above and adjacent to more resistive propylitic alteration (i.e. illite clays) in the reservoir. Moreover, the conductive clay cap also shows at its apex diagnostic fumarole areas (Coso Hot Springs and Devil's Kitchen).

Nevertheless there are limitations to this model. A key feature in the 3D resistivity model presented here that does not fit is the low-resistivity intrusive feature, confirmed by independent observations. Based on drilling, this area is highly fractured and very hot ( $> 250^{\circ}\text{C}$ ). Its low resistivity cannot be ascribed to conductive clays because of the temperature. We surmise that the low resistivity arises from large sets of fractures with fluids present in the vicinity.

A goal not yet achieved with this work was to conclusively show that 3D MT resistivity imaging could provide sufficient information to map and directly identify fractures containing geothermal fluids that could be drilled into. On a larger scale, however, the 3D model has detected some of the controlling features that influence location of subsurface fluids and well production, notably on the boundaries (faults) between mapped resistivity structures.

Another issue that could not be adequately addressed in this work is the problem of model equivalence (non-uniqueness), which continues to be a serious issue in the interpretation of MT data, especially in three dimensions. Without recourse to a good starting model, a 3D imaging experiment may not provide value added information. Many factors determine the quality of an image, including not only the starting model, but the type of noise in the data, the frequency band employed, spatial coverage and the robustness of the imaging algorithm. No doubt 3D MT imaging is and will be an ongoing research topic for years to come.

From the Coso experiment, we conclude that removal of static shifts in the data was very effective within the 3D inversion process, but activation of the deeper parts of the model space, below one km depth proved difficult without recourse to a good starting model. We believe there are ways to remedy this shortcoming by incorporating lower frequency data within the inversion process at the expense of larger grids and greater computational costs. Use of more effective depth-weighting schemes and preconditioning the inversion iteration may also be helpful and will be a subject of future studies. Nevertheless the focus of the current work is on an integrated interpretation of the Coso MT measurements and correlations with independent geophysical data sets, as well as geological and well information. We believe the major correlations found thus far are convincing enough and provide a level of confidence in the 3D resistivity model developed for the Coso system.

## Acknowledgements

Data collection and processing were supported under U.S. Department of Energy Contract DE-PS07-00ID1391 and U.S. Department of the Navy Contract N68936-03-P-0303 to the Energy and Geoscience Institute. We thank Coso Operating Company for access to the field and to the high-speed Internet services that made the ultra-distant remote referencing possible. Similarly we are grateful to New Mexico Institute of Mining and Technology (Prof. Harold Tobin) for providing a quiet reference site and fast ftp access. We also thank Frank Monastero, Steven Bjornstad and Allan Katzenstein of the U.S. Navy Geothermal Program office for support and encouragement, and for funding all archeological site clearances. Finally, the competence and diligence of the field crew of Quantec Geoscience, principally Jon Powell, Joel Cross, Claudia Moraga, Bill Doerner and Ken



Nurse, made results of this quality possible. Valuable discussions on MT data processing and use of the Parkfield facility were held with Gary Egbert (Oregon State University). The authors also thank Jeff Unruh for permission to present Figs. 2 and 3 in this paper, and the comprehensive review and editing of the paper by Marcelo Lippmann. The data interpretation carried out at Lawrence Berkeley National Laboratory was supported with funding provided by the U.S. Department of Energy Geothermal Program Office under Contract No. DE-AC02-05CH11231 with additional funding provided by the U.S. Department of the Navy contract N69218-05-P-00101.

## References

- Adams, M.C., Moore, J.N., Bjornstad, S., Norman, D.I., 2000. Geologic history of the Coso geothermal system. *Geothermal Resources Council Transactions* 24, 205–209.
- Anderson, E., Crosby, D., Ussher, G., 2000. Bulls-Eye!—simple resistivity imaging to reliably locate the geothermal reservoir. In: *Proceedings of the 2000 World Geothermal Congress, Kyushu–Tohoku, Japan, May 28–June 10*, pp. 909–914.
- Christensen, N.I., 1989. Seismic velocities. In: Carmichael, R.S. (Ed.), *Practical Handbook of Physical Properties of Rocks and Minerals*. CRC Press, Boca Raton, FL, USA, pp. 429–546.
- Cumming, W., Nordquest, G., Astra, D., 2000. Geophysical exploration for geothermal resources: an application for combined MT-TDEM. In: *Society of Exploration Geophysicists Annual Meeting Technical Program Expanded Abstracts*, 6–11 August, Calgary, Canada, pp. 1071–1074.
- de Lugao, P.P., Wannamaker, P.E., 1996. Calculating the two-dimensional magnetotelluric Jacobian in finite elements using reciprocity. *Geophysical Journal International* 127, 806–810.
- Dixon, T.H., Miller, M., Farina, F., Wang, H., Johnson, D., 2000. Present-day motion of the Sierra Nevada block and some tectonic implications for the Basin and Range province, North American Cordillera. *Tectonics* 19, 1–24.
- Egbert, G.D., 1997. Robust multiple station magnetotelluric data processing. *Geophysical Journal International* 130, 475–496.
- Garg, S.K., Pritchett, J.W., Wannamaker, P.E., Combs, J., 2007. Characterization of geothermal reservoirs with electrical surveys: Beowawe geothermal field. *Geothermics* 36, 487–517.
- Julian, B.R., Foulger, G.R., Richards-Dinger, K., 2004. The Coso geothermal area: a laboratory for advanced MEQ studies for geothermal monitoring. *GRC Transactions* 28, 403–405.
- Kurilovitch, L., Norman, D., Heizler, M., Moore, J., McCulloch, J., 2003. 40Ar/39Ar thermal history of the Coso geothermal field. In: *Proceedings of the Twenty-Eighth Workshop on Geothermal Reservoir Engineering*, Stanford University, pp. 110–116.
- Lees, J.M., Wu, H., 2000. Poisson's ratio and porosity at Coso geothermal area, California. *Journal of Volcanology and Geothermal Research* 95, 157–173.
- Lutz, S.J., Moore, J.N., Copp, J.F., 1996. Integrated mineralogical and fluid inclusion study of the Coso geothermal system, California. In: *Proceedings of the Twenty-First Workshop on Geothermal Reservoir Engineering*, Stanford University, pp. 187–194.
- Manley, C.R., Bacon, C.R., 2000. Rhyolite thermobarometry and the shallowing of the magma reservoir, Coso Volcanic Field, California. *Journal of Petrology* 41, 149–174.
- McClusky, S.C., Bjornstad, S.C., Hager, B.H., King, R.W., Meade, B.J., Miller, M.M., Monastero, F.C., Souter, B.J., 2001. Present day kinematics of the eastern California shear zone from a geodetically constrained block model. *Geophysical Research Letters* 28, 3369–3372.
- Monastero, F.C., Katzenstien, A.M., Miller, J.S., Unruh, J.R., Adams, M.C., Richards-Dinger, K., 2005. The Coso geothermal field: a nascent metamorphic core complex. *Geologic Society of America Bulletin* 117, 1534–1553.
- Newman, G.A., Alumbaugh, D.L., 2000. Three-dimensional magnetotelluric inversion using non-linear conjugate gradients. *Geophysical Journal International* 140, 410–424.
- Newman, G.A., Recher, S., Tezkan, B., Neubauer, F.M., 2003. 3D inversion of a scalar radio magnetotelluric field data set. *Geophysics* 68, 791–802.
- Palacky, G.J., 1987. Resistivity characteristics of geologic targets. In: Nabighian, M.N. (Ed.), *Electromagnetic Methods in Applied Geophysics*, vol. 1. Soc. Explor. Geophys., Tulsa, OK, USA, pp. 53–130.
- Rodi, W., Mackie, R.L., 2001. Nonlinear conjugate gradients algorithm for 2D magnetotelluric inversion. *Geophysics* 66, 174–187.

- Roquemore, G., 1980. Structure, tectonics, and stress field of the Coso Range, Inyo County, California. *Journal of Geophysical Research* 85, 2434–2440.
- Sanders, C.O., Ponko, S.C., Nixon, L.D., Schwartz, E.A., 1995. Seismological evidence for magmatic and hydrothermal structure in Long Valley caldera from local earthquake attenuation and velocity tomography. *J. Geophys. Res.* 100, 8311–8326.
- Schön, J.H., 1996. Physical properties of rocks: fundamentals and principles of petrophysics. In: Helbig, K., Treitel, S. (Eds.), *Handbook of Geophysical Exploration*, vol. 18. Pergamon, Terrytown, NY, USA, p. 583.
- Sheridan, J., Kovac, K., Rose, P., Barton, C., McCulloch, J., Berard, B., Moore, J., Petty, S., Spielman, P., 2003. In situ stress, fracture and fluid flow analysis—east flank of the Coso geothermal system. In: *Proceedings of the Twenty-Eight Workshop on Geothermal Reservoir Engineering*, Stanford University, pp. 34–49.
- Unruh, J.R., Hauksson, E., Monastero, F.C., Twiss, R.J., Lewis, J.C., 2002. Seismotectonics of the Coso Range-Indian Wells Valley region, California: transtensional deformation along the southeastern margin of the Sierran microplate. In: Glazner, A.F., Walker, J.D., Bartley, J.M. (Eds.), *Geologic Evolution of the Mojave Desert and Southwestern Basin and Range*, vol. 195. *Geol. Soc. Amer. Mem.*, pp. 277–294.
- Unruh, J.R., Monastero, F.C., Pullammanappallil, S.K., 2008. The nascent Coso metamorphic core complex, east-central California: brittle upper plate structure revealed by seismic reflection data. *International Geological Journal* 50, 1–25.
- Ussher, G., Harvey, C., Johnstone, R., Anderson, E., 2000. Understanding the Resistivities Observed in Geothermal Systems. In: *Proceedings of the 2000 World Geothermal Congress*, Kyushu-Tohoku, Japan, May 28–June 10, pp. 1915–1920.
- Vozoff, K., 1991. The magnetotelluric method. In: Nabighian, M.N. (Ed.), *Electromagnetic Methods in Applied Geophysics*, vol. 2B. Soc. Explor. Geophys., Tulsa, OK, USA, pp. 641–711.
- Wannamaker, P.E., 1997. Tensor CSAMT survey of the sulphur springs thermal area, Valles Caldera, New Mexico, Parts I&II: implications for structure of the Western Caldera and for CSAMT methodology. *Geophysics* 62, 451–476.
- Wannamaker, P.E., 1999. Affordable magnetotellurics: interpretation in natural environments. In: Oristaglio, M., Spies, B. (Eds.), *Three-dimensional Electromagnetics*. *Geophys. Devel. Ser.*, vol. 7. Soc. Explor. Geophys., Tulsa, OK, USA, pp. 349–374.
- Wannamaker, P.E., 2004. Creation of an enhanced geothermal system through hydraulic and thermal stimulation—magnetotelluric surveying and monitoring. Quarterly Project Information and Planning (PIP) Report, July 1–September 30, 2004, to the US Department of Wind and Geothermal Technologies, Enhanced Geothermal Systems Program, pp. 22–28.
- Wannamaker, P.E., Hohmann, G.W., Ward, S.H., 1984. Magnetotelluric responses of three-dimensional bodies in layered earths. *Geophysics* 49, 1517–1533.
- Wannamaker, P.E., Jiracek, G.R., Stodt, J.A., Caldwell, T.G., Porter, A.D., Gonzalez, V.M., McKnight, J.D., 2002. Fluid generation and movement beneath an active compressional orogen, the New Zealand Southern Alps, inferred from magnetotelluric (MT) data. *J. Geophys. Res.* 107 (B6), 1–22, ETG 6.
- Wannamaker, P.E., Johnston, J.M., Booker, J.R., Stodt, J.A., 1997. Anatomy of the Southern Cordilleran Hingeline, Utah and Nevada, from deep resistivity profiling. *Geophysics* 62, 1069–1086.
- Wannamaker, P.E., Rose, P., Doerner, W., Berard, B., McCulloch, J., Nurse, K., 2004. Magnetotelluric surveying and monitoring at the Coso geothermal area, California, in support of the enhanced geothermal systems concept: survey parameters and initial results. In: *Proceedings of the Twenty-Ninth Workshop on Geothermal Reservoir Engineering*, Stanford University, pp. 287–294.
- Wannamaker, P.E., Stodt, J.A., Rijo, L., 1987. A stable finite element solution for two-dimensional magnetotelluric modeling. *The Geophysical Journal of the Royal Astronomical Society* 88, 277–296.
- Whitmarsh, R.S., 2002. Geological map of the Cactus Peak 7.5' quadrangle, Inyo County, California, CD-ROM map. In: Glazner, A.F., Walker, J.D., Bartley, J.M. (Eds.), *Geologic Evolution of the Mojave Desert and Southwestern Basin and Range*. *Geol. Soc. Amer. Mem.*, p. 195.
- Wu, H., Lees, J.M., 1999. Three-dimensional *P* and *S* wave velocity structures of the Coso Geothermal Area, California, from microseismic travel time data. *J. Geophys. Res.* 104 (B6), 13217–13233.
- Zonge, K.L., Hughes, L.J., 1991. Controlled source audiomagnetotellurics. In: Nabighian, M.N. (Ed.), *Electromagnetic Methods in Applied Geophysics*, vol. 2B. Soc. Expl. Geophys., Tulsa, OK, USA, pp. 713–809.